



HAL
open science

Protonated hydrogen cyanide as a tracer of pristine molecular gas

Y. Gong, F J Du, C. Henkel, A. M. Jacob, A. Belloche, J.Z. Wang, K. M. Menten, W. Yang, D H Quan, C T Bop, et al.

► **To cite this version:**

Y. Gong, F J Du, C. Henkel, A. M. Jacob, A. Belloche, et al.. Protonated hydrogen cyanide as a tracer of pristine molecular gas. *Astronomy and Astrophysics - A&A*, 2023, *Astronomy and Astrophysics*, 679, pp.A39. 10.1051/0004-6361/202347409 . hal-04341933v1

HAL Id: hal-04341933

<https://hal.science/hal-04341933v1>

Submitted on 13 Dec 2023 (v1), last revised 13 Dec 2023 (v2)

HAL is a multi-disciplinary open access archive for the deposit and dissemination of scientific research documents, whether they are published or not. The documents may come from teaching and research institutions in France or abroad, or from public or private research centers.

L'archive ouverte pluridisciplinaire **HAL**, est destinée au dépôt et à la diffusion de documents scientifiques de niveau recherche, publiés ou non, émanant des établissements d'enseignement et de recherche français ou étrangers, des laboratoires publics ou privés.



Distributed under a Creative Commons Attribution 4.0 International License

Protonated hydrogen cyanide as a tracer of pristine molecular gas[★]

Y. Gong¹, F. J. Du^{2,3}, C. Henkel^{1,4,5}, A. M. Jacob^{6,1}, A. Belloche¹, J. Z. Wang⁷, K. M. Menten¹,
W. Yang¹, D. H. Qian^{8,5}, C. T. Bop⁹, G. N. Ortiz-León¹⁰, X. D. Tang^{5,11,12}, M. R. Rugel^{13,14,1}, and S. Liu¹⁵

¹ Max-Planck-Institut für Radioastronomie, Auf dem Hügel 69, 53121 Bonn, Germany
e-mail: ygong@mpi-fr-bonn.mpg.de

² Purple Mountain Observatory, Chinese Academy of Sciences, 10 Yuanhua Road, Qixia District, Nanjing 210023, PR China

³ School of Astronomy and Space Science, University of Science and Technology of China, 96 JinZhai Road, Baohe District, Hefei 230026, PR China

⁴ Astronomy Department, Faculty of Science, King Abdulaziz University, PO Box 80203, Jeddah 21589, Saudi Arabia

⁵ Xinjiang Astronomical Observatory, Chinese Academy of Sciences, 150 Science 1-Street, Urumqi, Xinjiang 830011, PR China

⁶ William H. Miller III Department of Physics & Astronomy, Johns Hopkins University, 3400 North Charles Street, Baltimore, MD 21218, USA

⁷ Guangxi Key Laboratory for Relativistic Astrophysics, Department of Physics, Guangxi University, 100 Daxuedong Road, Nanning 530004, PR China

⁸ Research Center for Intelligent Computing Platforms, Zhejiang Laboratory, Hangzhou 311100, PR China

⁹ Univ. Rennes, CNRS, IPR (Institut de Physique de Rennes) – UMR 6251, 35000 Rennes, France

¹⁰ Instituto Nacional de Astrofísica, Óptica y Electrónica, Apartado Postal 51 y 216, Puebla 72000, Mexico

¹¹ Key Laboratory of Radio Astronomy, Chinese Academy of Sciences, 150 Science 1-Street, Urumqi 830011, PR China

¹² University of Chinese Academy of Sciences, Beijing 100049, PR China

¹³ Center for Astrophysics – Harvard & Smithsonian, 60 Garden St., Cambridge, MA 02138, USA

¹⁴ National Radio Astronomy Observatory, 1003 Lopezville RD, Socorro, NM 87801, USA

¹⁵ National Astronomical Observatories, Chinese Academy of Sciences, 20A Datun Road, Chaoyang District, Beijing 100101, PR China

Received 9 July 2023 / Accepted 29 August 2023

ABSTRACT

Context. Protonated hydrogen cyanide, HCNH⁺, plays a fundamental role in astrochemistry because it is an intermediary in gas-phase ion-neutral reactions within cold molecular clouds. However, the impact of the environment on the chemistry of HCNH⁺ remains poorly understood.

Aims. We aim to study HCNH⁺, HCN, and HNC, as well as two other chemically related ions, HCO⁺ and N₂H⁺, in different star formation regions in order to investigate how the environment influences the chemistry of HCNH⁺.

Methods. With the IRAM 30 m and APEX 12 m telescopes, we carried out HCNH⁺, H¹³CN, HN¹³C, H¹³CO⁺, and N₂H⁺ imaging observations toward two dark clouds, the Serpens filament and Serpens South, both of which harbor sites of star formation that include protostellar objects and regions that are quiescent.

Results. We report the first robust distribution of HCNH⁺ in the Serpens filament and in Serpens South. Our data suggest that HCNH⁺ is abundant in cold and quiescent regions but is deficient in active star-forming regions. The observed HCNH⁺ fractional abundances relative to H₂ range from 3.1×10^{-11} in protostellar cores to 5.9×10^{-10} in prestellar cores, and the HCNH⁺ abundance generally decreases with increasing H₂ column density, which suggests that HCNH⁺ coevolves with cloud cores. Our observations and modeling results suggest that the abundance of HCNH⁺ in cold molecular clouds is strongly dependent on the H₂ number density. The decrease in the abundance of HCNH⁺ is caused by the fact that its main precursors (e.g., HCN and HNC) undergo freeze-out as the number density of H₂ increases. However, current chemical models cannot explain other observed trends, such as the fact that the abundance of HCNH⁺ shows an anticorrelation with that of HCN and HNC but a positive correlation with that of N₂H⁺ in the southern part of Serpens South's northern clump. This indicates that additional chemical pathways have to be invoked for the formation of HCNH⁺ via molecules such as N₂ in regions in which HCN and HNC freeze out.

Conclusions. Both the fact that HCNH⁺ is most abundant in molecular cores prior to gravitational collapse and the fact that low-*J* HCNH⁺ transitions have very low H₂ critical densities make this molecular ion an excellent probe of pristine molecular gas.

Key words. ISM: clouds – radio lines: ISM – astrochemistry – ISM: molecules – ISM: abundances

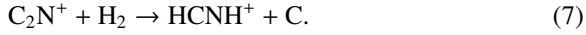
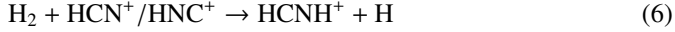
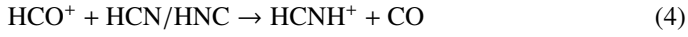
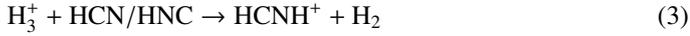
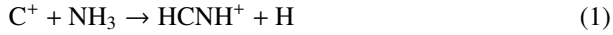
1. Introduction

Protonated hydrogen cyanide, or iminomethylum (HCNH⁺), is one of the fundamental molecular ions in the interstellar medium. Ions play an important role in interstellar chemistry

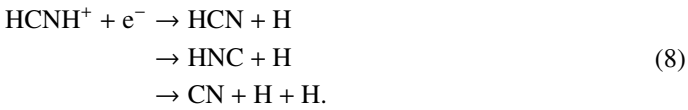
as essential intermediaries in the ion-neutral reactions that dominate gas-phase chemistry in cold molecular clouds (e.g., [Agúndez & Wakelam 2013](#), and references therein). The chemistry of HCNH⁺ in dense and cold regions has been extensively investigated. This ion is mainly produced by ion-neutral reactions ([Turner et al. 1990](#); [Schilke et al. 1991](#); [Herbst et al. 2000](#); [Loison et al. 2014a](#); [Quénard et al. 2017](#); [Fontani et al. 2021](#)),

* The reduced FITS cubes are available at <https://zenodo.org/records/10027118>

for instance



On the other hand, HCNH^+ is thought to be mainly destroyed by dissociative recombination reactions:



Reactions (8) are exothermic, which suggests that HCNH^+ is the main precursor of CN, HCN, and HNC (Herbst & Klemperer 1973; Herbst 1978). The chemical pathway of forming CN is energetically unfavorable in cold molecular clouds because the simultaneous dissociation of the C-H and N-H bonds requires two electron excitations (e.g., Shiba et al. 1998). Theoretical and observational studies support the notions that reactions (8) are the main pathways to HCN and HNC (e.g., Shiba et al. 1998; Hirota et al. 1998; Aalto et al. 2002), and that the branching ratios to produce HCN and HNC are nearly identical at low temperatures (e.g., Mendes et al. 2012; Loison et al. 2014a; Fontani et al. 2021).

HCNH^+ is a simple linear molecule with a small dipole moment of 0.29 D (Botschwina 1986). It was first discovered in Sgr B2 via the detection of its three lowest rotational transitions (Ziurys & Turner 1986) and was subsequently observed in many other dense molecular clouds (e.g., Schilke et al. 1991; Ziurys et al. 1992; Hezareh et al. 2008; Quénard et al. 2017; Fontani et al. 2021). This suggests that HCNH^+ is ubiquitous in molecular clouds.

Due to the nonzero nuclear spin of nitrogen, HCNH^+ transitions show electric quadrupole hyperfine structure (HFS) splitting. Spectra in which the HFS of the HCNH^+ $J = 1 - 0$ transition is resolved have been presented, for example by Ziurys et al. (1992) for TMC1¹ and by Quénard et al. (2017) for L1544, which are both chemically well-studied dark clouds. Fontani et al. (2021) performed a survey of HCNH^+ (3–2) toward 26 high-mass star-forming cores and report the detection of this molecule in 16 targets. Their study and the ones mentioned above suggest that the typical fractional abundance of HCNH^+ with respect to H_2 spans a range of two orders of magnitude, from 10^{-11} to 3×10^{-9} . Quénard et al. (2017) find that the observed HCNH^+ and HC_3NH^+ abundances in the dark cloud L1544 could not be well reproduced at the same time by astrochemical models, indicating that the chemistry related to HCNH^+ is still not fully understood. Numerical simulations suggest that observations of the chemically coevolving pair, HCN and HCNH^+ , could be used to measure the ion-neutral drift velocity caused

by ambipolar diffusion (Tritsis et al. 2023), which plays an important role in star formation (e.g., Mouschovias & Ciolek 1999). In addition, HCNH^+ has also been suggested to be an intermediate species in the formation of formamide in the solid phase (Kerkeni & Simmie 2023).

Measurements using the Cassini space probe indicate that HCNH^+ may also be the most abundant ion in the atmosphere of the largest satellite of Saturn, Titan (Cravens et al. 2006). This molecular ion was not detected in Comet Hale-Bopp (also known as C/1995 O1; Ziurys et al. 1999). These authors reported an upper limit of $1.9 \times 10^{13} \text{ cm}^{-2}$ for its column density and an abundance ratio $[\text{HCN}]/[\text{HCNH}^+] \geq 1$ in this comet. Given all this, a thorough understanding of the chemistry of HCNH^+ in molecular clouds is still elusive but essential for us to gain insights into the process of chemical evolution of the interstellar medium and star formation.

Observations have shown that the environment of star-forming regions can strongly affect their chemistry (e.g., Jørgensen et al. 2020). However, the influence of the environment on the HCNH^+ fractional abundance is still unknown. From an observational perspective, single-pointing studies of dense cores can result in loose constraints, whereas mapping studies can better address this issue. So far, HCNH^+ has only rarely been mapped. Because HCNH^+ (3–2) is blended with an unidentified line at 222325 MHz (possibly from CH_3OCH_3) in the study of Sgr B2 in Schilke et al. (1991) due to the broad line widths, the map of the blended line cannot be used to reliably trace the distribution of HCNH^+ in this cloud. Therefore, the spatial distribution of HCNH^+ in molecular clouds remains largely unexplored.

At a distance of ~440 pc (Dzib et al. 2010; Ortiz-León et al. 2017, 2018, 2023; Zucker et al. 2019), Serpens South and the Serpens filament are known as two of the nearest infrared dark clouds. Both only harbor low-mass young stellar objects (YSOs; e.g., Gutermuth et al. 2008; Gong et al. 2018) and both contain parts that are quiescent as well as parts with active star formation (e.g., Friesen et al. 2013; Gong et al. 2021), which allows us to probe the influence of star formation on the chemistry.

Serpens South contains one of the nearest and youngest stellar protoclusters, the Serpens South cluster (SSC), while its northern clump (referred to as SSN hereafter) is quiescent. There are powerful outflows arising in the SSC (e.g., Nakamura et al. 2011, 2014; Plunkett et al. 2015a,b; Zhang et al. 2015; Mottram et al. 2017), and the H_2O masers are located at the base of one of them (Ortiz-León et al. 2021). In contrast, the SSN is found to have high abundances of carbon-chain molecules (Friesen et al. 2013, 2016; Li et al. 2016); even benzonitrile, $c\text{-C}_6\text{H}_5\text{CN}$, has recently been detected (Burkhardt et al. 2021).

A similar trend is also observed in the Serpens filament, which is quiescent in the southeast and shows signs of star formation in the northwest (Gong et al. 2018, 2021). Star formation in Serpens South is much more active than in the Serpens filament, which allows us to probe different levels of star formation feedback on the chemistry. Furthermore, the two regions have typical line widths of $\lesssim 2 \text{ km s}^{-1}$ (e.g., Levshakov et al. 2013, 2014; Friesen et al. 2016; Gong et al. 2021); this reduces the level of line confusion, which can be a significant problem for observations of the HCNH^+ (3–2) transition in regions such as Sgr B2 (Schilke et al. 1991). Therefore, the Serpens filament and Serpens South are ideal sites to study the influence of the environment on the HCNH^+ fractional abundance. In this work we present a mapping study of HCNH^+ to unveil its distribution and characterize its chemistry in these two regions.

¹ TMC1 harbors two chemically different dense cores, which are known as the cyanopolyne peak and the ammonia peak (e.g., Toelle et al. 1981; Pratap et al. 1997). Throughout this paper, when we refer to TMC1, we mean the cyanopolyne peak, toward which the spectrum shown by Ziurys et al. (1992) was taken, rather than the ammonia peak.

Table 1. Observational and spectroscopic parameters related to the molecular lines presented in this work.

Transition	Frequency (MHz)	E_u/k (K)	A (s ⁻¹)	μ (D)	$n_c(\text{H}_2)$ (cm ⁻³)	θ_{beam} ($''$)	$\eta_{\text{mb}}/\eta_{\text{f}}$	Serpens filament		Serpens South		Telescope
								σ (mK)	δv (km s ⁻¹)	σ (mK)	δv (km s ⁻¹)	
(1)	(2)	(3)	(4)	(5)	(6)	(7)	(8)	(9)	(10)	(11)	(12)	(13)
HCNH ⁺ $J = 1 - 0$	74 111.302(3)	3.6	1.4×10^{-7}	0.29	2.0×10^2	33	0.87	–	–	51	0.20	IRAM-30 m
HCNH ⁺ $J = 2 - 1$	148 221.450(17)	10.7	1.3×10^{-6}	0.29	1.7×10^3	18	0.78	21	0.21	58	0.21	IRAM-30 m
HCNH ⁺ $J = 3 - 2$	222 329.277(8)	21.3	4.9×10^{-6}	0.29	5.2×10^3	27	0.80	28	0.08	20	0.08	APEX
H ¹³ CN $J = 1 - 0$	86 339.921(1)	4.1	2.2×10^{-5}	2.99	5.3×10^5	28	0.85	22	0.17	24	0.68	IRAM-30 m
HN ¹³ C $J = 1 - 0$	87 090.825(4)	4.2	1.9×10^{-5}	2.70	1.4×10^5	28	0.85	18	0.17	26	0.67	IRAM-30 m
H ¹³ CO ⁺ $J = 1 - 0$	86 754.288(5)	4.2	3.9×10^{-5}	3.90	6.2×10^4	28	0.85	40	0.17	27	0.68	IRAM-30 m
N ₂ H ⁺ $J = 1 - 0$	93 173.398(1)	4.5	3.6×10^{-5}	3.40	6.1×10^4	26	0.84	19	0.16	26	0.63	IRAM-30 m

Notes. (1) Observed transition. All transitions were observed in on-the-fly mode except for HCNH⁺ (3–2), which was observed as a single pointing toward Serpens South. (2) Rest frequency taken from the Cologne Database for Molecular Spectroscopy (CDMS, <https://cdms.astro.uni-koeln.de/>; Endres et al. 2016). Uncertainties in the last digits are given in parentheses. For the observed lines, only the frequency of the strongest HFS component is listed. (3) Upper energy level of the observed transition. (4) Einstein A coefficient. (5) Dipole moment from CDMS (Endres et al. 2016). (6) Optically thin H₂ critical density at a kinetic temperature of 10 K. The critical densities of HCNH⁺ transitions are calculated using the collisional rate coefficients from Bop & Lique (2023) and Eq. (4) in Shirley (2015). For the other lines, the values are directly taken from Table 1 in Shirley (2015). The critical density of HN¹³C (1–0) is assumed to be the same as that of HNC (1–0). (7) HPBW. (8) η_{f} and η_{mb} are the forward efficiency and main beam efficiency, respectively. (9) RMS level at the smoothed angular resolution of 36 $''$.3. (10) Velocity channel spacing. (11) RMS level at the smoothed angular resolution of 36 $''$.3. For pointed HCNH⁺ (3–2) observations in Serpens South, the RMS level is estimated at the original angular resolution of 27 $''$. (12) Velocity channel spacing. (13) Telescope.

Our observations are described in Sect. 2. In Sect. 3 we report our results, which are discussed in Sect. 4. Lastly, our summary and conclusions are presented in Sect. 5.

2. Observations and data reduction

2.1. IRAM 30 m and APEX 12 m observations

We carried out HCNH⁺ (1–0), HCNH⁺ (2–1), H¹³CN (1–0), HN¹³C (1–0), H¹³CO⁺ (1–0), and N₂H⁺ (1–0) imaging observations toward Serpens South and the Serpens filament with the Institut de Radioastronomie Millimétrique (IRAM) 30 m telescope² during the following periods: 2019 September 27–29, 2020 December 26–27, 2021 August 21–24, and October 22–25. During the observations, the Eight Mixer Receiver (EMIR) dual-sideband and dual-polarization receivers (E090 and E150) were used as frontend (Carter et al. 2012), while fast Fourier transform spectrometers (FFTSs) were used as backend. For the HCNH⁺ (1–0) and HCNH⁺ (2–1) lines, we used the narrow FFTSs, which provided a channel width of 50 kHz, corresponding to a velocity spacing of 0.2 km s⁻¹ at 74 GHz and 0.1 km s⁻¹ at 148 GHz (see also Table 1). For H¹³CN (1–0), HN¹³C (1–0), H¹³CO⁺ (1–0), and N₂H⁺ (1–0), FFTSs with a channel width of 50 kHz and 250 kHz are used for the Serpens filament and Serpens South, respectively. The corresponding channel spacings in units of km s⁻¹ are given in Table 1.

Using the Atacama Pathfinder EXperiment (APEX³) 12 meter submillimeter telescope (Güsten et al. 2006), we carried out HCNH⁺ (3–2) mapping observations toward the Serpens filament from 2019 April 29 to May 1 (project code: M9511A_103)

² This work is based on observations carried out under project numbers 023-19, 127-20, 028-21 with the IRAM 30 m telescope. IRAM is supported by INSU/CNRS (France), MPG (Germany) and IGN (Spain).

³ This publication is based on data acquired with the Atacama Pathfinder Experiment (APEX). APEX is a collaboration between the Max-Planck-Institut für Radioastronomie, the European Southern Observatory, and the Onsala Space Observatory.

and pointed HCNH⁺ (3–2) observations toward Serpens South from 2018 May 25 to 2018 July 13 (project code: M9506A_101). The coordinates of the pointed positions are given in Table 2. A PI230 sideband separated and dual-polarization receiver⁴, built by the Max Planck Institute for Radio Astronomy, was employed as frontend, while FFTSs were adopted as backend (Klein et al. 2012). Each FFTS encompasses a bandwidth of 4 GHz and 65536 channels, resulting in a channel width of 61 kHz. The corresponding velocity spacing is 0.08 km s⁻¹ for HCNH⁺ (3–2) (see also Table 1). The observations were performed in position-switching or on-the-fly modes using the APECS software (Muders et al. 2006).

At the beginning of each observing session, pointing and focus were investigated toward bright continuum sources like Mars and Mercury. Pointing was regularly checked on nearby bright sources every hour, and its accuracy was found to be within 5 $''$. A single on-off observation toward the SSC was performed to verify each frequency setup before mapping. The regions were observed in two orthogonal directions using the On-The-Fly mode. The standard chopper wheel method was used for calibrations and correcting the atmospheric attenuation of the IRAM 30 m observations (Ulich & Haas 1976), while an extension of the method using three loads was applied to the APEX 12 m observations. The calibration was undertaken about every 10 min. The antenna temperature, T_{A}^* , was converted to main beam temperature, T_{mb} , by applying the relation, $T_{\text{mb}} = T_{\text{A}}^* \eta_{\text{f}} / \eta_{\text{mb}}$, where η_{f} and η_{mb} are the forward efficiency and main beam efficiency⁵, respectively (see Table 1 for the values). The uncertainties in the absolute flux calibration are assumed to be 10% in this work. The observed spectral lines, their rest frequencies, and other spectroscopic and observational information are listed in Table 1. Velocities with respect to the local standard of rest (LSR) are reported throughout this work.

⁴ <https://www.eso.org/public/teles-instr/apex/pi230/>

⁵ See <https://publicwiki.iram.es/Iram30mEfficiencies> and <http://www.apex-telescope.org/telescope/efficiency/>

Table 2. Spectral line properties of the HCNH⁺ (3–2) transition observed toward the selected positions in Serpens South.

Name	α_{J2000} (h m s)	δ_{J2000} (° ' ")	T_p (mK)	v_{lsr} (km s ⁻¹)	Δv (km s ⁻¹)	Class	Other names
(1)	(2)	(3)	(4)	(5)	(6)	(7)	(8)
KAM280	18:29:57.50	-01:58:43.7	485 ± 33	7.57 ± 0.01	0.47 ± 0.02	Prestellar	SerpS-MM9
KAM281	18:29:57.72	-01:57:58.2	245 ± 30	7.55 ± 0.01	0.58 ± 0.03	Prestellar	SerpS-MM8
KAM283	18:29:58.20	-02:01:15.2	52 ± 18	7.55 ± 0.01	1.49 ± 0.34	Prestellar	
KAM284	18:29:58.66	-02:08:22.5	<67	–	–	Prestellar	
KAM289	18:30:00.85	-02:06:57.3	<56	–	–	Protostellar	SerpS-MM11
KAM292	18:30:01.50	-02:10:25.5	<56	–	–	Protostellar	SerpS-MM13, IRAS 18274-0212
KAM293	18:30:02.13	-02:08:15.1	<55	–	–	Prestellar	SerpS-MM14
KAM294	18:30:02.77	-02:01:03.4	79 ± 25	7.28 ± 0.06	1.15 ± 0.12	Prestellar	SerpS-MM15
KAM299	18:30:04.19	-02:03:05.5	39 ± 5	7.49 ± 0.05	1.16 ± 0.11	Protostellar	SERS 02, SerpS-MM18
KAM309	18:30:07.24	-02:12:13.6	84 ± 10	6.25 ± 0.04	0.44 ± 0.09	Prestellar	
KAM315	18:30:12.44	-02:06:53.6	169 ± 21	6.69 ± 0.02	0.80 ± 0.05	Protostellar	SerpS-MM22

Notes. (1) Source name from Könyves et al. (2015). (2) Right ascension. (3) Declination. (4) Peak main beam brightness temperature. (5) Velocity centroid. (6) FWHM line width. (7) Classification from Könyves et al. (2015). (8) Other names from Maury et al. (2011) and Mottram et al. (2017).

The GILDAS⁶ software was used to reduce the spectral line data (Pety 2005), and a first-order baseline was subtracted from each spectrum. For all the maps, raw spectra were gridded into a data cube with a pixel size of 5''×5''. Since the HCNH⁺ emission in our sources is generally weak and has a smooth extent, all spectral data are smoothed to a half power beam width (HPBW) of 36''/3. This facilitates the comparison with the *Herschel* H₂ column density and dust temperature maps (see Sect. 2.2).

2.2. Archival data

Dust-based H₂ column density and dust temperature maps⁷ were derived from spectral energy distributions fitted to *Herschel* data at four far-infrared bands, that is, 160, 250, 350, and 500 μm (André et al. 2010; Könyves et al. 2015; Fiorellino et al. 2021). These maps also have an angular resolution of 36''/3.

NH₃ and CO archival data are only available for Serpens South. For NH₃ in Serpens South, we utilized the data products⁸ from observations with the Green Bank Telescope (Friesen et al. 2016). The corresponding HPBW is 32''. CO (3–2) data⁹ of Serpens South were obtained with the Atacama Submillimeter Telescope Experiment (ASTE) 10 m telescope. The data that we retrieved has a HPBW of 22'' and a channel width of ~0.11 km s⁻¹. The typical noise level is 0.11 K on a T_A^* scale at a velocity spacing of 0.5 km s⁻¹. The main beam efficiency is 0.57 at 345 GHz. Details of the observations are presented in Nakamura et al. (2011).

3. Results

3.1. Molecular distribution

Figure 1 presents the distributions of HCNH⁺ (2–1) and HCNH⁺ (3–2) emission toward the Serpens filament. The overall distributions of the two transitions are similar in the Serpens

⁶ <https://www.iram.fr/IRAMFR/GILDAS/>

⁷ http://www.herschel.fr/cea/gouldbelt/en/Phoce/Vie_des_labos/Ast/ast_visu.php?id_ast=66

⁸ <https://dataverse.harvard.edu/dataset.xhtml?persistentId=doi:10.7910/DVN/SDHQRP>

⁹ <http://th.nao.ac.jp/MEMBER/nakamrfm/sflegacy/data.html>

filament, with slight differences arising from the fact that the signal-to-noise ratio of HCNH⁺ (3–2) is lower than that of HCNH⁺ (2–1). HCNH⁺ is detected toward three dense cores, called bolo2, bolo4, and bolo12 by Enoch et al. (2007). The name “bolo” refers to Bolocam that is a large-format bolometric camera of the Caltech Submillimeter Observatory (Glenn et al. 2003). The emission is the brightest in bolo4 followed by bolo12. Based on the comparison with the *Herschel* results, we find that the detected HCNH⁺ emission arises from regions with dust temperatures, T_d , of ≤12 K and H₂ column densities >1×10²² cm⁻² (Fiorellino et al. 2021), which indicates that the observed HCNH⁺ emission mainly arises from cold and high H₂ column density regions. Toward the YSO emb10¹⁰, which drives a molecular outflow (Gong et al. 2021, 2023, see also Figs. 1c,d for the outflow lobes), the HCNH⁺ emission appears to be absent.

Figure 2 presents the distribution of HCNH⁺ (2–1) emission toward Serpens South with the purple crosses marking the positions of the prestellar dense cores extracted from the *Herschel* dust continuum maps (Könyves et al. 2015). We find that the HCNH⁺ emission is prominent toward the SSN, but barely detected toward the SSC. The brightest HCNH⁺ emission lies in the southern part of the SSN (labeled as SSN1 in Fig. 2b), which is slightly offset from the dust continuum peak (the prestellar core KAM280, No. 280 in Könyves et al. 2015, also named SerS MM9 by Maury et al. 2011). The emission in the northern part of the SSN (labeled as SSN2 in Fig. 2b) and the weak emission in the SSC appear not to be associated with any dust continuum core. The detected HCNH⁺ emission in the SSN comes from regions with T_d ≤12 K, similar to those in the Serpens filament. We also note that the weak HCNH⁺ emission in the SSC arises from a slightly warmer region with T_d ~15 K. The ammonia observations (Friesen et al. 2016) confirm that the gas kinetic temperatures are ≤12 K in the SSN and ~15 K in the SSC. On the other hand, the HCNH⁺ emitting region in Serpens South has H₂ column densities ≥4×10²² cm⁻². In Fig. 2d, the weak HCNH⁺ emission in the SSC appears to coincide with the peak of the redshifted outflow lobe (Nakamura et al. 2011) that is about 30'' offset from the H₂ column density peak. However, the observed line width of the weak emission is as narrow as

¹⁰ The term “emb” is the abbreviation of “embedded” (Enoch et al. 2009).

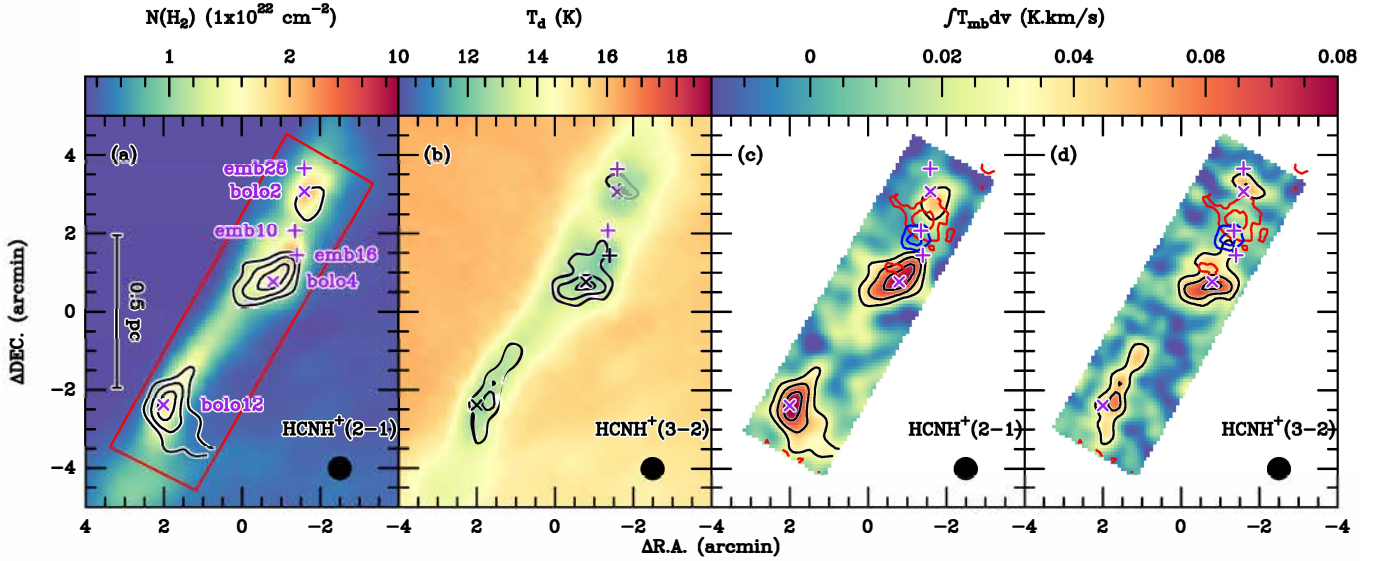


Fig. 1. Distribution of HCNH⁺ in the Serpens filament. (a) *Herschel* H₂ column density map of the Serpens filament (Fiorellino et al. 2021) overlaid with the HCNH⁺ (2–1) integrated intensity contours. The velocity range over which the HCNH⁺ (2–1) intensity map is integrated is 7.7–8.7 km s^{−1}. The contours start at 0.03 K km s^{−1} (3σ) and increase in steps of 0.02 K km s^{−1}. The red boundary represents the region mapped by our IRAM 30 m and APEX 12 m observations. (b) *Herschel* dust temperature map (Fiorellino et al. 2021) overlaid with the HCNH⁺ (3–2) integrated intensity contours. The velocity range over which the HCNH⁺ (3–2) intensity is integrated is 7.7–8.7 km s^{−1}. The contours start at 0.03 K km s^{−1} (3σ) and increase in steps of 0.02 K km s^{−1}. (c) HCNH⁺ (2–1) integrated intensity map overlaid with the blueshifted and redshifted outflow lobes of ¹³CO (2–1) that are driven by emb10 (Gong et al. 2021). The black contours are the same as in panel a. (d) Similar to panel c, but for HCNH⁺ (3–2). The beam size is shown in the lower-right corner of each panel. In all panels, the (0, 0) offset corresponds to α_{J2000}=18^h28^m50^s.4, δ_{J2000}=00°49′58″.72. The three purple plus signs indicate the positions of the three embedded YSOs, emb10, emb16, and emb 28 (Enoch et al. 2009), while the three purple crosses mark the positions of three 1.1 mm dust continuum cores, bolo2, bolo4, and bolo12 (Enoch et al. 2007).

0.45 ± 0.21 km s^{−1}, which does not suggest that the weak HCNH⁺ emission is produced by the outflow shocks.

As shown in Fig. 3, our APEX 12 m pointed observations toward Serpens South have led to the detection of HCNH⁺ (3–2) in seven dense cores with $T_d \leq 18$ K. The brightest HCNH⁺ (3–2) emission comes from KAM280, which is in agreement with our HCNH⁺ (2–1) map. The detection of HCNH⁺ (3–2) in KAM299 (also known as SerS-MM18) suggests that HCNH⁺ exists in the SSC, but that its emission is much weaker than in the SSN. The observed line profiles are commonly Gaussian-like. In order to derive the observational parameters, we employed a single-Gaussian component to fit the observed spectra, because the HFS lines of the 3–2 transition are too close in frequency to be separated. The fitted peak main beam brightness temperature, velocity centroids, and full width at half maximum (FWHM) line widths are given in Table 2.

We also mapped Serpens South in HCNH⁺ (1–0) but no emission was detected. This places a 3σ upper limit of 0.15 K for the peak intensity. In order to detect the weak HCNH⁺ (1–0) emission, we average all the HCNH⁺ (1–0) spectra in the region where the HCNH⁺ (2–1) integrated intensities are higher than 3σ. The results are shown in Fig. 4. The HCNH⁺ (1–0) average spectrum has a ~5σ detection and peaks at exactly the same velocity as its HCNH⁺ (2–1) counterpart, securing the detection of HCNH⁺ (1–0). However, the contributions of the HFS satellite lines are not discernible in Fig. 4 at the current noise level. The detected lines are mainly attributed to the contributions of the $F = 2 - 1$ and $F = 3 - 2$ hyperfine lines for $J = 1 - 0$ and $J = 2 - 1$, respectively.

In this work we use H¹³CN (1–0), HN¹³C (1–0), H¹³CO⁺ (1–0), and N₂H⁺ (1–0) emission as proxies to investigate the distributions of HCN, HNC, HCO⁺, and N₂H⁺ emission toward the Serpens filament and Serpens South. The Serpens filament

has been mapped in N₂H⁺ (1–0) by Gong et al. (2018). Serpens South has been mapped in N₂H⁺ (1–0) and H¹³CO⁺ (1–0) by Kirk et al. (2013) and Tanaka et al. (2013). In comparison to these studies, the observations presented here provide either higher angular resolutions or better sensitivities, or both. Figures 5–6 present the integrated intensity maps of HCNH⁺, H¹³CN, HN¹³C, H¹³CO⁺, and N₂H⁺. Comparing the distribution of HCNH⁺ with those of the other tracers in the Serpens filament (see Fig. 5), we find that the different tracers have nearly the same distribution toward bolo12, which is not affected by star formation. Toward bolo4, the distribution of HCNH⁺ is similar to those of H¹³CN and HN¹³C, but is slightly different from those of H¹³CO⁺ and N₂H⁺ (i.e., the peaks of the H¹³CO⁺ and N₂H⁺ emission lie to the west of the HCNH⁺ emission peak). Since bolo4 lies close to the blueshifted outflow lobe from emb10 (see Fig. 1), the difference could be caused by outflow feedback.

In Serpens South (Fig. 6) HCNH⁺ emission is weak toward the SSC. This is in stark contrast to the other four tracers, which exhibit the brightest emission toward the SSC. Toward the SSN, the molecular morphologies are different for the various molecular gas tracers, which is more evident in Fig. 7. No molecular line emission peaks at the positions of the dust peaks. The HCNH⁺ emission peaks are offset from the emission peaks of other molecular line tracers, which could be (at least partially) caused by selective freeze-out processes and optical depth effects, as discussed further in Sect. 3.2.

3.2. Molecular column densities and abundances

Based on the HFS fit to the N₂H⁺ (1–0) spectra, we find that the total optical depth of N₂H⁺ (1–0) is generally larger than unity in our mapped regions. Therefore, we first apply the HFS

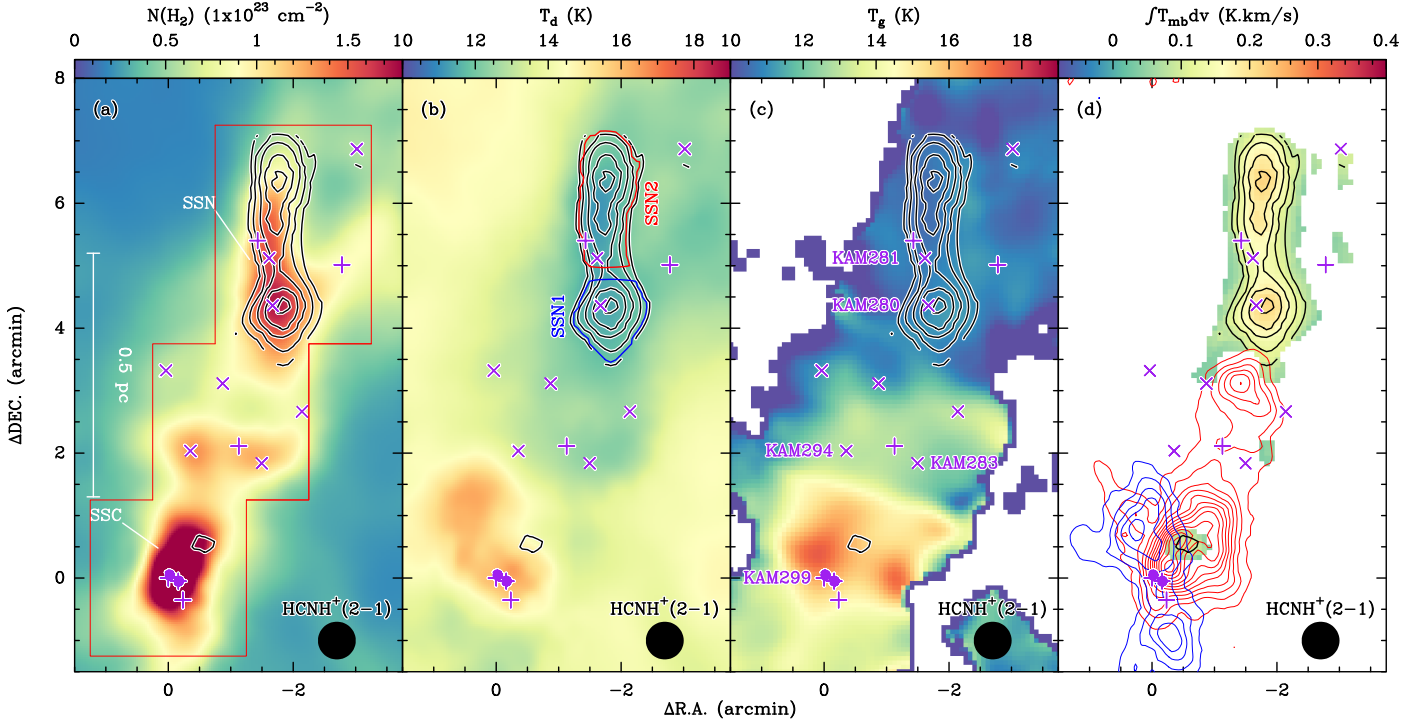


Fig. 2. Distribution of HCNH^+ in Serpens South. (a) *Herschel* H_2 column density map of Serpens South (Könyves et al. 2015) overlaid with HCNH^+ (2–1) integrated intensity contours. The velocity range over which the HCNH^+ (2–1) intensity is integrated is $6.5\text{--}8.5\text{ km s}^{-1}$. The contours start at 0.09 K km s^{-1} (3σ) and increase in steps of 0.03 K km s^{-1} . The red boundary represents the region mapped by our IRAM 30 m observations. (b) *Herschel* dust temperature map (Könyves et al. 2015) overlaid with the HCNH^+ (2–1) integrated intensity contours that are the same as in panel a. The SSN is further divided into two subregions, SSN1 and SSN2, which are labeled in this panel. (c) Gas kinetic temperature map derived from ammonia observations (Friesen et al. 2016) overlaid with the HCNH^+ (2–1) integrated intensity contours, which are the same as in panel a. (d) HCNH^+ (2–1) integrated intensity map overlaid with the CO (3–2) blueshifted and redshifted outflow lobes from the SSC (Nakamura et al. 2011). The black contours represent HCNH^+ (2–1) integrated intensity and are the same as the contours in panel a. The beam size is shown in the lower-right corner of each panel. In all panels, the (0, 0) offset corresponds to $\alpha_{J2000}=18^{\text{h}}30^{\text{m}}04^{\text{s}}.19$, $\delta_{J2000}=-02^{\circ}03'05''.5$. The two purple circles represent the two 22 GHz water masers (Ortiz-León et al. 2021). The purple pluses indicate the positions of deeply embedded YSOs (Könyves et al. 2015; Sun et al. 2022), while the purple crosses mark the positions of the prestellar dense cores extracted from the *Herschel* dust continuum maps (Könyves et al. 2015).

fit to the N_2H^+ (1–0) data cube with the PySpecKit package (Ginsburg & Mirocha 2011) to obtain the excitation temperature, total optical depth, velocity centroid, and velocity dispersion. We discard the fitted results for spectra with excitation temperatures lower than 5σ in order to have reliable measurements of the derived column densities. The results are shown in Figs. 8 and 9. We find that the N_2H^+ (1–0) excitation temperatures are generally lower than 7 K in the Serpens filament, and 3.3–11.1 K in Serpens South. The highest excitation temperature of 11.1 K is found toward the SSC. This is expected, because the SSC tends to have the highest kinetic temperature and H_2 column density (see Fig. 2). The total optical depths of N_2H^+ (1–0) become quite high toward bolo4 in the Serpens filament and the SSN in Serpens South, with the highest total optical depths reaching up to ~ 14.5 and ~ 24.5 in bolo4 and the SSN, respectively. Figures 8c and 9c present the distributions of the velocity dispersions of the N_2H^+ emission, which further support our hypothesis that the HCNH^+ emission is more prominent toward the quiescent regions that have velocity dispersions $\leq 0.3\text{ km s}^{-1}$.

With the fitted values, the N_2H^+ column densities can be estimated using Eq. (95) from Mangum & Shirley (2016),

$$N_{\text{tot}} = \frac{3h}{8\pi^3\mu^2S} \frac{Q(T_{\text{ex}})}{g_J} \exp\left(\frac{E_u}{kT_{\text{ex}}}\right) \left[\exp\left(\frac{h\nu}{kT_{\text{ex}}}\right) - 1 \right]^{-1} \times \int \tau dv, \quad (9)$$

where h is the Planck constant, μ is the dipole moment (see Table 1), S is the line strength, $Q(T_{\text{ex}})$ is the molecular partition function at the excitation temperature, T_{ex} , g_J describes the rotational degeneracy, E_u is the upper level energy of the transition, T_{bg} is the background temperature that is set to be 2.73 K here (Fixsen 2009), and $\int \tau dv$ is the integrated optical depth. For linear molecules, the line strength of a transition is given as $S = \frac{J_u}{2J_u+1}$ and the rotational degeneracy is given as $g_J = 2J_u + 1$, where J_u is the total angular momentum of the upper level of a given transition in a two-level system. The partition function of linear molecules can be approximated as $Q(T_{\text{ex}}) = \frac{kT_{\text{ex}}}{hB} + \frac{1}{3}$, where B is the rotational constant.

With this equation, we are able to derive the column densities of N_2H^+ . The results are shown in Figs. 8d and 9d. The derived N_2H^+ column densities are $(0.4\text{--}10.8)\times 10^{12}\text{ cm}^{-2}$ and $(0.8\text{--}57.1)\times 10^{12}\text{ cm}^{-2}$ for the Serpens filament and Serpens South, respectively. It is worth noting that the distribution of N_2H^+ column densities is slightly different from the corresponding N_2H^+ (1–0) integrated intensity map, which is caused by the optical depths of N_2H^+ (1–0) and the variations of excitation temperature. Furthermore, the HCNH^+ emission peaks coincide with the peaks of N_2H^+ column densities toward bolo2, bolo4, bolo12, and the peak in SSN2 in Figs. 8d and 9d, which implies that HCNH^+ can, similarly to N_2H^+ , trace prestellar core centers in such regions.

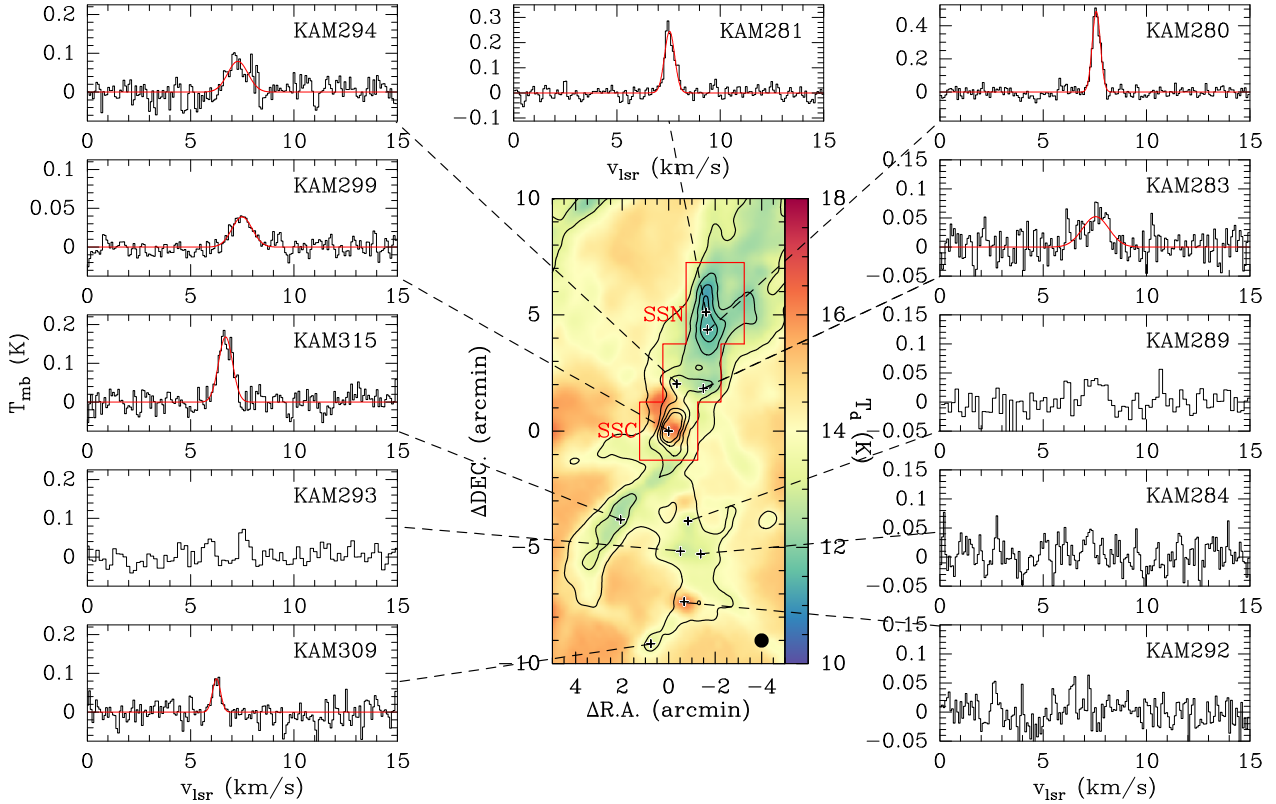


Fig. 3. *Herschel* dust temperature map of Serpens South (Könyves et al. 2015) overlaid with H_2 column density contours that start at $2 \times 10^{22} \text{ cm}^{-2}$ and increase in steps of $2 \times 10^{22} \text{ cm}^{-2}$. The beam size is shown in the lower-right corner of the central panel. The (0, 0) offset corresponds to $\alpha_{J2000} = 18^{\text{h}}30^{\text{m}}04^{\text{s}}.19$, $\delta_{J2000} = -02^{\circ}03'05''.5$. The region mapped in HCNH^+ (2–1) is indicated by the red boundary. The positions toward which pointed observations of HCNH^+ (3–2) were carried out are indicated by the black plus signs in Serpens South. Observed HCNH^+ (3–2) spectra are displayed in black, while Gaussian fits to the line profiles are shown in red. The source name is indicated in the upper-right corner of each panel.

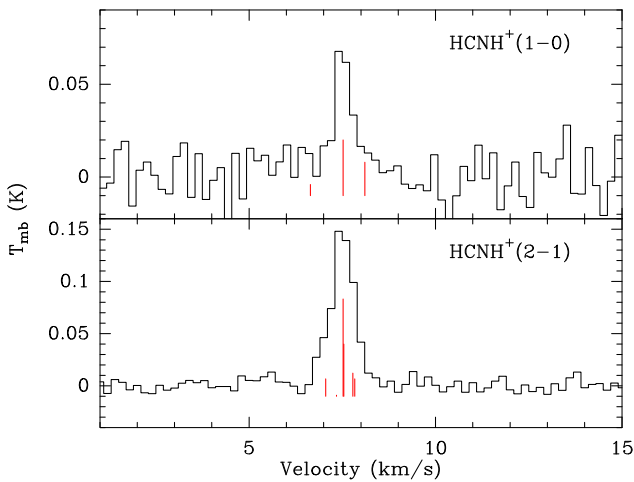


Fig. 4. HCNH^+ (1–0) and HCNH^+ (2–1) spectra averaged over the region where HCNH^+ (2–1) integrated intensities are higher than 3σ in Fig. 2. The positions and relative intensities of the HFS components are indicated by the vertical red lines.

Based on the HFS fit to H^{13}CN (1–0), we find that its total optical depths can reach up to about 3. However, the HFS fitting toward the whole data cube tends to have large uncertainties for most pixels, which makes most of the fitting results unreliable. This could be caused by the anomalous line intensities of the hyperfine lines (e.g., Walmsley et al. 1982;

Cernicharo et al. 1984; Loughnane et al. 2012; Jin et al. 2015; Goicoechea et al. 2022) and the relatively low signal-to-noise ratios. In order to balance the signal-to-noise ratio and optical depth effect, we use the $F = 2 - 1$ satellite line (5/9 of the total optical depths) of H^{13}CN (1–0) to estimate H^{13}CN column densities in the optically thin approximation.

As for HCNH^+ , the peak intensities of its (2–1) and (3–2) lines are typically <0.5 K. Adopting a beam dilution factor of unity and an excitation temperature of 12 K, their peak optical depths are lower than 0.1 according to the radiative transfer equation. This suggests that HCNH^+ (2–1) and (3–2) are optically thin.

We performed a similar estimate for HN^{13}C (1–0) and H^{13}CO^+ (1–0). We find that these lines' peak optical depths can be higher than unity. HN^{13}C (1–0) also has HFS components, but these components are too close in frequency to allow for an accurate determination of its optical depth. Hence, HN^{13}C (1–0) and H^{13}CO^+ (1–0) were simply assumed to be optically thin in this study. Assuming conditions of local thermodynamic equilibrium (LTE) and using the optically thin approximation, we can therefore estimate the beam-averaged column densities of these molecules. Nevertheless, we must exercise caution when interpreting the resulting H^{13}CN , HN^{13}C , and H^{13}CO^+ column densities in regions with high peak intensities, as they can be only taken as the lower limits in case of high optical depths.

Excitation temperatures are needed to determine the molecular column densities. In the optically thin regime, the HCNH^+ excitation temperature can be estimated from the line ratio between HCNH^+ (2–1) and (3–2). Because of the relatively

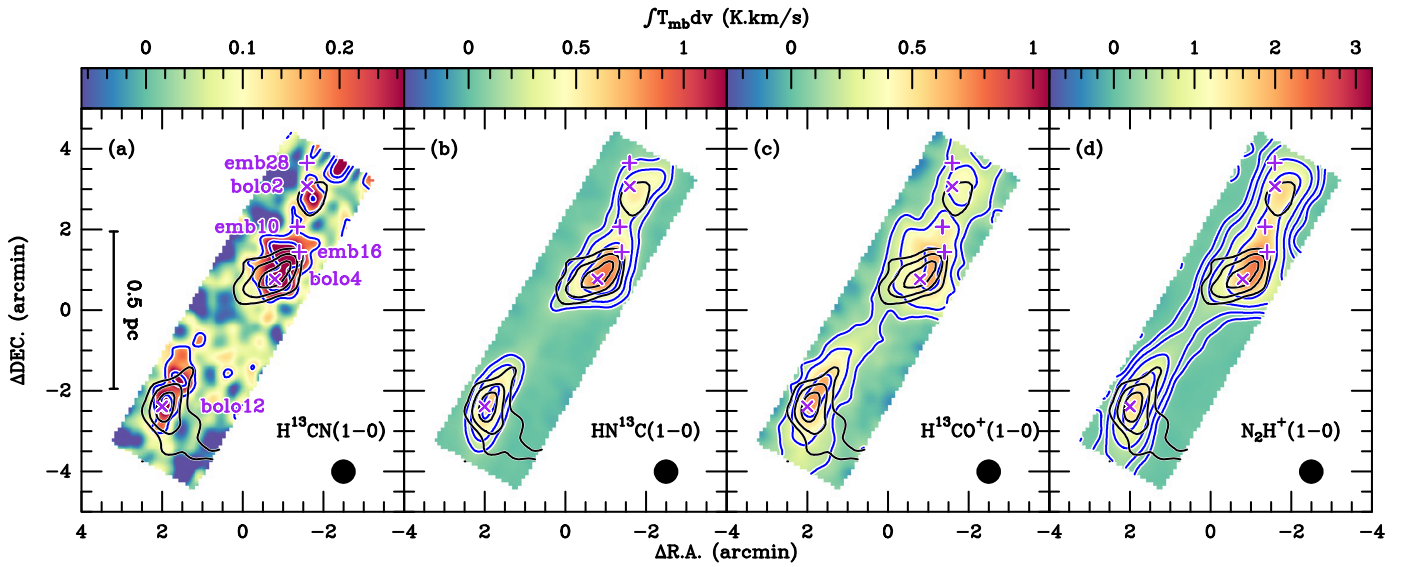


Fig. 5. Comparison of different tracers in the Serpens filament. Integrated-intensity maps (on a color scale) of (a) H^{13}CN (1–0), (b) HN^{13}C (1–0), (c) H^{13}CO^+ (1–0), and (d) N_2H^+ (1–0). The blue contours represent the respective integrated intensities, which are $2'' \times 0.15 \text{ K km s}^{-1}$ and $n = 0, 1, 2, \dots$. The black contours of HCNH^+ (2–1) integrated intensities are the same as in Fig. 1a. The intensity was integrated over $7\text{--}9.5 \text{ km s}^{-1}$ for HN^{13}C (1–0) and H^{13}CO^+ (1–0), while a broader velocity range ($5\text{--}9.5 \text{ km s}^{-1}$) was chosen to cover the three main HFS components of N_2H^+ (1–0). The beam size is shown in the lower-right corner of each panel. In all panels, the (0, 0) offset corresponds to $\alpha_{J2000} = 18^{\text{h}}28^{\text{m}}50^{\text{s}}.4$, $\delta_{J2000} = 00^{\circ}49'58''.72$. The markers are the same as in Fig. 1.

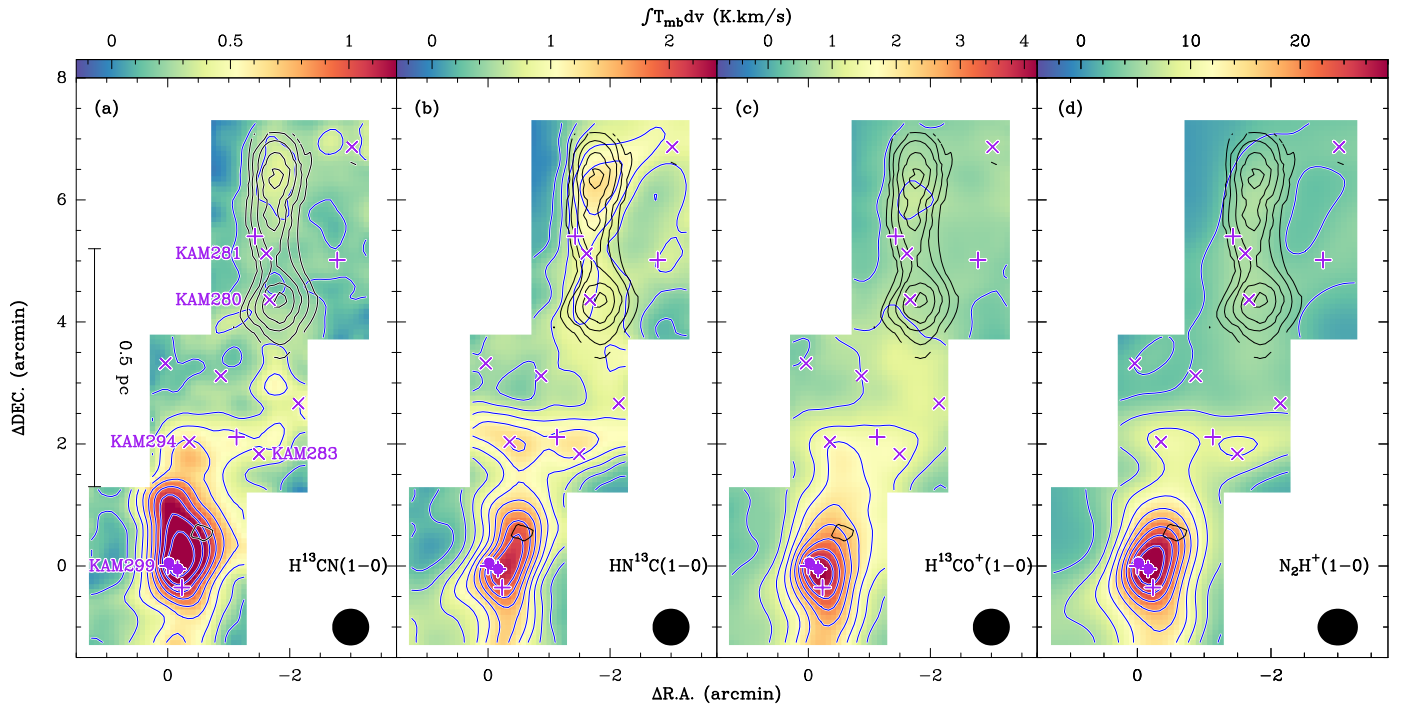


Fig. 6. Comparison of different tracers in Serpens South. Integrated-intensity maps (on a color scale) of (a) H^{13}CN (1–0), (b) HN^{13}C (1–0), (c) H^{13}CO^+ (1–0), and (d) N_2H^+ (1–0). The blue contours represent the respective integrated intensities. They vary from 10% to 90% of the peak integrated intensities in steps of 10%, where the peak integrated intensities are 1.57 K km s^{-1} , 2.25 K km s^{-1} , 4.26 K km s^{-1} , and $30.24 \text{ K km s}^{-1}$ for H^{13}CN (1–0), HN^{13}C (1–0), H^{13}CO^+ (1–0), and N_2H^+ (1–0), respectively. The black contours of HCNH^+ (2–1) integrated intensities are the same as in Fig. 2a. The intensity was integrated over $7\text{--}9.5 \text{ km s}^{-1}$ for H^{13}CN (1–0), HN^{13}C (1–0), and H^{13}CO^+ (1–0), while a broader range ($5\text{--}9.5 \text{ km s}^{-1}$) was chosen to cover the three main HFS components of N_2H^+ (1–0). The beam size is shown in the lower-right corner of each panel. In all panels, the (0, 0) offset corresponds to $\alpha_{J2000} = 18^{\text{h}}30^{\text{m}}04^{\text{s}}.19$, $\delta_{J2000} = -02^{\circ}03'05''.5$. The markers are the same as in Fig. 2.

low signal-to-noise ratios in the HCNH^+ images, we only estimate the excitation temperatures toward emission peaks. Toward bolo12 and bolo4 in the Serpens filament, we obtain excitation

temperatures of $\sim 7 \text{ K}$ and $\sim 18 \text{ K}$, respectively. Toward KAM280, we convolved the HCNH^+ (2–1) raw data of Serpens South to an angular resolution of $27''$ to match the angular resolution

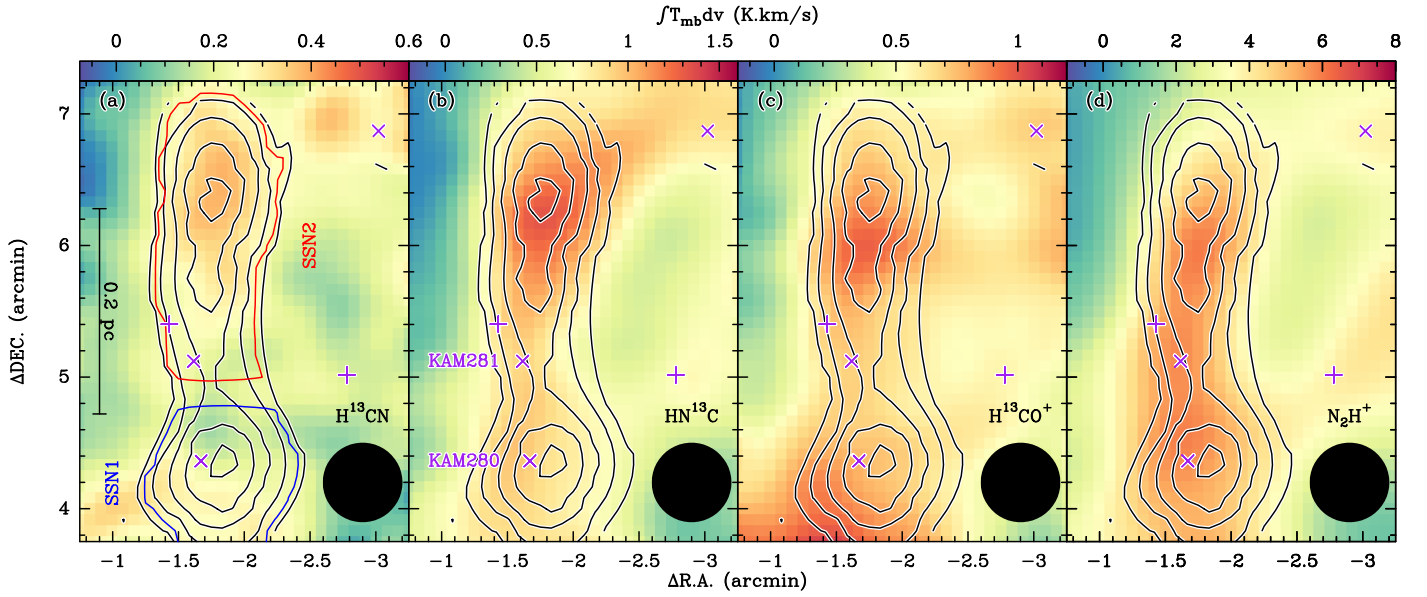


Fig. 7. Same as Fig. 6 but zoomed in on the SSN with different color scales for better visualization. The two subregions, SSN1 and SSN2, are labeled in panel a.

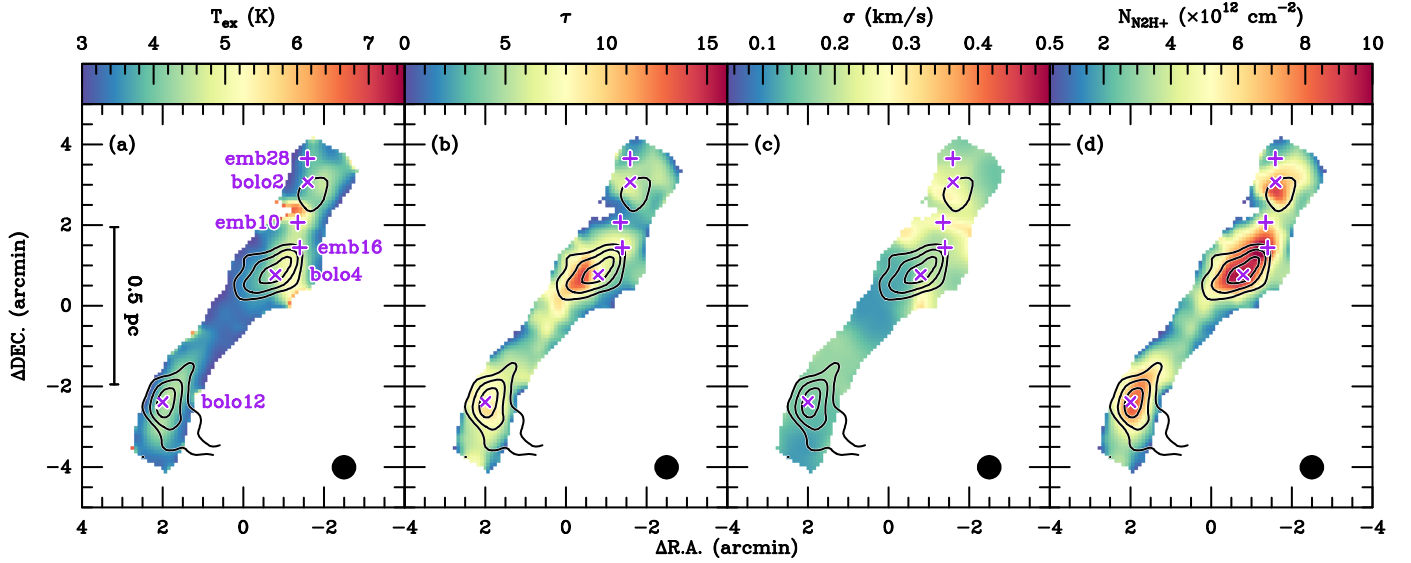


Fig. 8. Distributions of the fitted properties of N_2H^+ (1–0) in the Serpens filament. (a) N_2H^+ (1–0) excitation temperature, (b) total optical depth, (c) velocity dispersion, and (d) N_2H^+ column density. The overlaid HCNH^+ (2–1) integrated-intensity contours are the same as in Fig. 1a.

of the HCNH^+ (3–2) spectra and then derived the line ratio, which indicates an excitation temperature of ~ 12 K. The integrated intensity ratio between HCNH^+ (2–1) and HCNH^+ (1–0) is ~ 2 in the averaged spectra (see Fig. 4), corresponding to an excitation temperature of ~ 10 K. The excitation temperatures are close to the gas kinetic temperature derived from ammonia (e.g., Friesen et al. 2016). These estimates imply that the excitation temperatures might vary within the range of 7–18 K. In the following analysis, we assume a constant excitation temperature of 12 K in order to derive the column density of HCNH^+ . Considering an excitation temperature range of 7–18 K, the assumption of a fixed excitation temperature can introduce uncertainties in the derived HCNH^+ column densities of at most 15%. Making use of the excitation temperature, we made a fit to the

HCNH^+ (3–2) data of KAM299 in Fig. 10, which demonstrates that our sensitivities are not sufficient to detect HCNH^+ (1–0) and (2–1).

Because H^{13}CN (1–0), HN^{13}C (1–0), and H^{13}CO^+ (1–0) have quite high critical densities (see Table 1), these transitions are likely sub-thermal. Hence, we adopt a lower excitation temperature of 5 K for H^{13}CN (1–0), HN^{13}C (1–0), and H^{13}CO^+ (1–0). This assumption is consistent with the excitation temperature assumed for these species in previous studies toward dark clouds (e.g., Hirota et al. 1998). If the excitation temperature is as high as 10 K, the derived column densities are underestimated by only $\sim 6\%$ for H^{13}CN , HN^{13}C , and H^{13}CO^+ . Using the assumed excitation temperatures, we can calculate the column densities of HCNH^+ , H^{13}CN , HN^{13}C , and H^{13}CO^+ from HCNH^+ (2–1),

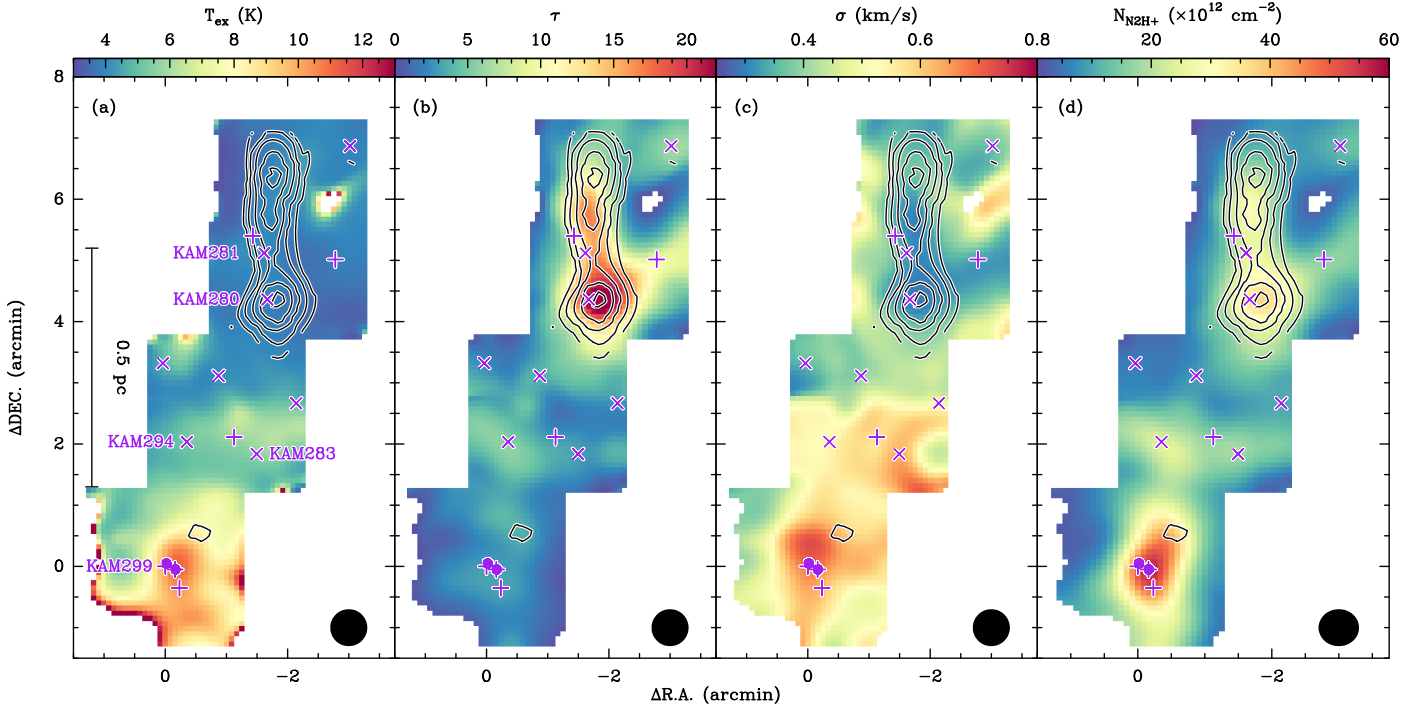


Fig. 9. Distributions of the fitted properties of N_2H^+ (1–0) in Serpens South. (a) N_2H^+ (1–0) excitation temperature, (b) total optical depth, (c) velocity dispersion, and (d) N_2H^+ column density. The red pixels at the southern boundary of panel a have large uncertainties for the fitted excitation temperatures. The overlaid HCNH^+ (2–1) integrated-intensity contours are the same as in Fig. 2a.

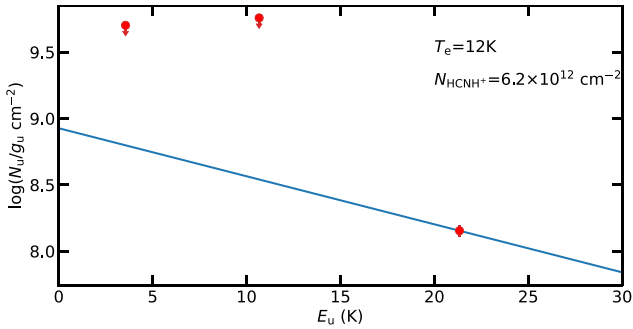


Fig. 10. Population diagram of HCNH^+ toward KAM299. The blue line represents the fit expected from the excitation temperature and HCNH^+ column density, which are given in the top-right corner.

H^{13}CN (1–0), HN^{13}C (1–0), and H^{13}CO^+ (1–0), respectively. The distributions of these molecular column densities are shown in Appendix A. The derived column densities are listed in Table 3, where the errors were estimated through a Monte Carlo analysis. In this analysis, we estimate the uncertainties in the column densities derived by generating 10 000 realizations randomly sampled from the Gaussian distributions associated with integrated intensities, optical depths, and line widths, propagating these samples through through Eq. (9), and then analyzing the resulting distribution of outcomes to estimate the uncertainties.

Molecular abundances, $X(\text{A}) = N(\text{A})/N(\text{H}_2)$, are derived from the ratio between molecular column densities, $N(\text{A})$, and H_2 column densities, $N(\text{H}_2)$, by adopting the *Herschel* dust-based H_2 column density maps (Könyves et al. 2015; Fiorellino et al. 2021). The derived molecular abundances are listed in Table 4, and the statistical results of the derived molecular abundances are presented in Fig. 11. Compared to TMC1 and L1544 (Caselli et al. 2002a,b; Agúndez & Wakelam 2013; Quénard et al. 2017; Hirota et al. 1998), we find that the H^{13}CN , HN^{13}C , and

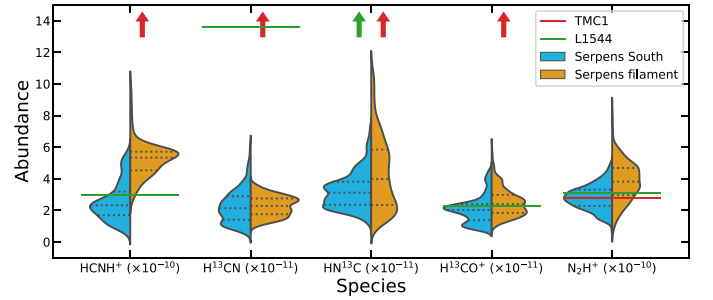


Fig. 11. Comparison of the fractional abundances of different species with respect to H_2 determined on a pixel-by-pixel basis. The y -axis has been divided by the scaling values, which are given in parentheses after the molecule names along the x -axis for better visualization. The dotted lines indicate the 25%, 50%, and 75% percentiles of the respective distributions. The molecular abundances in TMC1 and L1544 are also indicated for comparison. The arrows indicate that their abundances are higher than the maximum value on the y -axis.

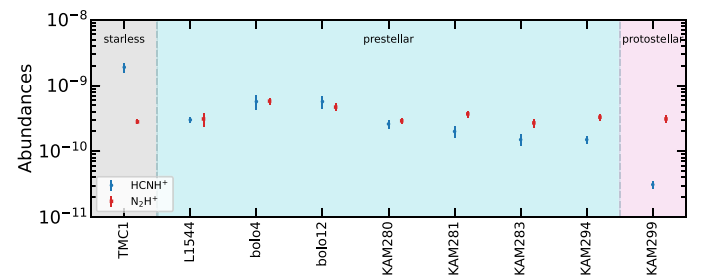


Fig. 12. HCNH^+ (blue) and N_2H^+ (red) abundances relative to H_2 as a function of evolutionary stages.

Table 3. Molecular column densities of the observed targets.

Name	T_d (K)	T_g (K)	$N(\text{H}_2)$ ($\times 10^{22} \text{ cm}^{-2}$)	$N(\text{HCNH}^+)^{(*)}$ ($\times 10^{12} \text{ cm}^{-2}$)	$N(\text{H}^{13}\text{CN})^{(*)}$ ($\times 10^{11} \text{ cm}^{-2}$)	$N(\text{HN}^{13}\text{C})^{(*)}$ ($\times 10^{11} \text{ cm}^{-2}$)	$N(\text{H}^{13}\text{CO}^+)^{(*)}$ ($\times 10^{11} \text{ cm}^{-2}$)	$N(\text{N}_2\text{H}^+)$ ($\times 10^{12} \text{ cm}^{-2}$)
(1)	(2)	(3)	(4)	(5)	(6)	(7)	(8)	(9)
The Serpens filament	12.0–16.3	...	0.3–2.2	5.1–10.3	1.1–6.3	0.7–18.2	0.6–7.0	0.4–10.8
bolo4	12.4	...	1.7	9.7 ± 2.1	6.1 ± 1.1	17.9 ± 0.3	5.8 ± 0.2	10.0 ± 0.7
bolo12	12.5	...	1.8	10.1 ± 1.8	4.7 ± 0.5	12.9 ± 0.1	6.7 ± 0.2	8.3 ± 0.5
Serpens South	11.1–16.5	10.3–17.5	1.8–16.7	4.2–27.1	2.5–46.8	1.9–45.0	1.1–41.2	0.8–57.1
KAM280	11.4	10.9	9.6	24.8 ± 2.3	6.3 ± 0.3	18.7 ± 0.3	7.5 ± 0.2	35.1 ± 2.0
KAM281	11.6	10.7	8.6	17.1 ± 2.4	6.7 ± 0.4	18.0 ± 0.3	6.8 ± 0.1	24.7 ± 1.5
KAM283	12.4	12.6	6.6	10.8 ± 1.8	12.9 ± 0.4	23.2 ± 0.5	14.6 ± 0.3	17.7 ± 1.4
KAM294	13.4	12.9	7.3	12.6 ± 1.3	20.1 ± 0.4	26.8 ± 0.5	16.2 ± 0.2	23.9 ± 1.4
KAM299	16.0	16.4	16.4	6.2 ± 0.5	42.2 ± 0.3	37.3 ± 0.9	37.3 ± 0.9	50.6 ± 2.2

Notes. (1) Source name. (2) Dust temperature. (3) Gas kinetic temperature. “...” indicates that no information is available. (4) H_2 column density. (5) HCNH^+ column density. For KAM283, KAM294, and KAM299 where HCNH^+ (2–1) emission is not detected, we use HCNH^+ (3–2) to estimate the column densities at a resolution of $27''$. (6) H^{13}CN column density. (7) HN^{13}C column density. (8) H^{13}CO^+ column density. (9) N_2H^+ column density. “***” indicates that these column densities are derived under the optically thin assumption. A constant excitation temperature of 12 K is assumed for HCNH^+ , while a constant excitation temperature of 5 K is assumed for H^{13}CN , HN^{13}C , and H^{13}CO^+ .

Table 4. Molecular abundances with respect to H_2 toward different targets.

Name	$X(\text{HCNH}^+)$ ($\times 10^{-10}$)	$X(\text{H}^{13}\text{CN})$ ($\times 10^{-11}$)	$X(\text{HN}^{13}\text{C})$ ($\times 10^{-11}$)	$X(\text{H}^{13}\text{CO}^+)$ ($\times 10^{-11}$)	$X(\text{N}_2\text{H}^+)$ ($\times 10^{-10}$)
(1)	(2)	(3)	(4)	(5)	(6)
The Serpens filament	2.5–10.1	1.3–3.8	0.9–11.0	(0.9–6.1)	0.6–8.6
bolo4	5.7 ± 1.4	3.6 ± 0.8	10.5 ± 0.1	3.4 ± 0.4	5.8 ± 0.7
bolo12	5.7 ± 1.2	2.7 ± 0.4	7.2 ± 0.8	3.8 ± 0.4	4.7 ± 0.6
Serpens South	0.3–5.9	0.4–3.7	0.9–7.4	0.7–4.7	0.5–5.2
KAM280	2.6 ± 0.4	0.7 ± 0.1	2.0 ± 0.2	0.8 ± 0.1	2.9 ± 0.3
KAM281	2.0 ± 0.4	0.8 ± 0.1	2.1 ± 0.2	0.8 ± 0.1	3.7 ± 0.4
KAM283	1.5 ± 0.3	2.0 ± 0.2	3.5 ± 0.4	2.2 ± 0.2	2.7 ± 0.4
KAM294	1.5 ± 0.2	2.7 ± 0.3	3.7 ± 0.4	2.2 ± 0.2	3.3 ± 0.4
KAM299	0.31 ± 0.04	2.6 ± 0.3	2.3 ± 0.2	2.3 ± 0.2	3.1 ± 0.4
TMC1	19.0 ± 3.0	17.8 ± 2.1	41.7 ± 6.2	14.4 ± 0.3	2.8 ± 0.2
L1544	3.0 ± 0.3	13.6 ± 1.7	31.4 ± 5.7	2.3 ± 0.7	3.1 ± 0.7

Notes. (1) Source name. (2) HCNH^+ fractional abundance relative to H_2 . (3) H^{13}CN fractional abundance relative to H_2 . (4) HN^{13}C fractional abundance relative to H_2 . (5) H^{13}CO^+ fractional abundance relative to H_2 . (6) N_2H^+ fractional abundance relative to H_2 . The uncertainties of molecular abundances are estimated by assuming 10% uncertainties in the dust-based H_2 column densities (Könyves et al. 2015). The molecular abundances in TMC1 are taken from Pratap et al. (1997) and Schilke et al. (1991), while the molecular abundances in L1544 are based on Caselli et al. (2002a,b), Quénard et al. (2017), and Hirota et al. (1998).

H^{13}CO^+ abundances are lower in Serpens South and the Serpens filament (see Fig. 11). On the other hand, the derived N_2H^+ abundances in TMC1 and L1544 are comparable to those of our mapped regions, which suggests that N_2H^+ abundances do not vary much in different environments. For HCNH^+ , the molecular abundances vary from 6.5×10^{-11} to 5.9×10^{-10} with a median value of 2.4×10^{-10} and 5.6×10^{-10} in Serpens South and the Serpens filament, respectively. These values are comparable to that in L1544 ($\sim 3 \times 10^{-10}$; Quénard et al. 2017) but lower than that of TMC1 ($\sim 1.9 \times 10^{-9}$; Schilke et al. 1991) and generally higher than the abundances measured in high-mass star formation regions ($0.9\text{--}14 \times 10^{-11}$; Fontani et al. 2021).

We further investigate the HCNH^+ abundance variation as a function of evolutionary stage in Fig. 12, which suggests that the HCNH^+ abundance decreases by almost two

orders of magnitude from the starless phase to the protostellar phase. This finding is consistent with the results toward high-mass star formation regions where the decrease in the HCNH^+ abundance is attributed to an evolutionary effect (Fontani et al. 2021).

The spatial distributions of molecular fractional abundances are shown in Figs. 13 and 14. In Fig. 13, H^{13}CO^+ abundances peak toward the west of the dust continuum peak in bolo4. In contrast, HCNH^+ , HN^{13}C , H^{13}CN , and N_2H^+ can still trace the core center of bolo4. It is expected that H^{13}CO^+ would not be a reliable tracer of the core center in bolo4, as CO, which is a main precursor of HCO^+ , has been observed to undergo depletion in this region (Gong et al. 2018, 2021). This is consistent with the fact that CO freezes out onto dust grains for cold and dense regions.

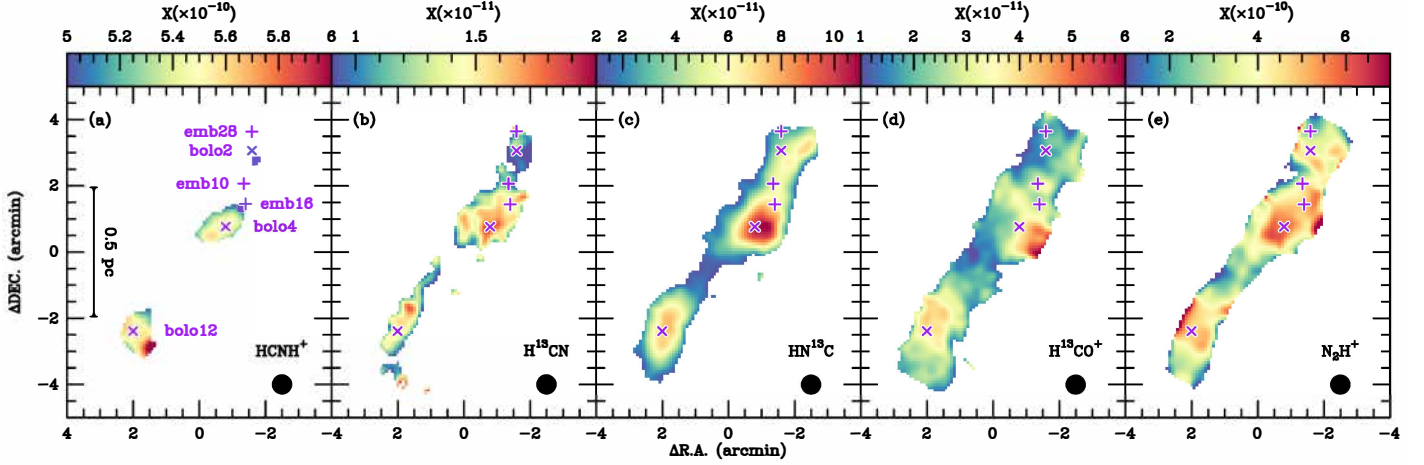


Fig. 13. Molecular abundance distributions in the Serpens filament. (a) HCNH^+ , (b) H^{13}CN , (c) HN^{13}C , (d) H^{13}CO^+ , and (e) N_2H^+ . The beam size is shown in the lower-right corner of each panel. In all panels, the (0, 0) offset corresponds to $\alpha_{J2000}=18^{\text{h}}28^{\text{m}}50^{\text{s}}.4$, $\delta_{J2000}=00^{\circ}49'58''.72$. The markers are the same as in Fig. 1.

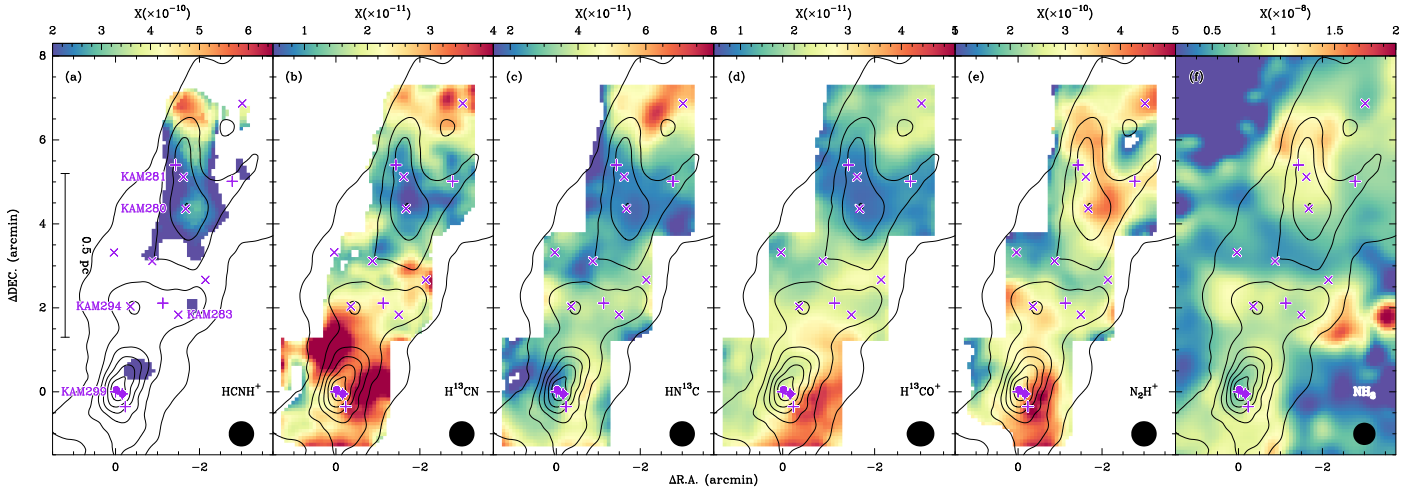


Fig. 14. Molecular abundance distributions in Serpens South. (a) HCNH^+ , (b) H^{13}CN , (c) HN^{13}C , (d) H^{13}CO^+ , (e) N_2H^+ , and (f) para- NH_3 (from Friesen et al. 2016). The overlaid *Herschel* dust-based H_2 column density contours start at $2.4 \times 10^{22} \text{ cm}^{-2}$ and increase in steps of $2.4 \times 10^{22} \text{ cm}^{-2}$. The beam size is shown in the lower-right corner of each panel. In all panels, the (0, 0) offset corresponds to $\alpha_{J2000}=18^{\text{h}}30^{\text{m}}04^{\text{s}}.19$, $\delta_{J2000}=-02^{\circ}03'05''.5$. The markers are the same as in Fig. 2.

In Fig. 14, we find that the molecular fractional abundances of HCNH^+ , H^{13}CN , HN^{13}C , H^{13}CO^+ are lower in the southern part of SSN2 than the northern part of SSN2 by a factor of ≥ 2 , which suggests a north-south abundance gradient across SSN2. The H^{13}CN , HN^{13}C , H^{13}CO^+ abundances are even lower in SSN1. This could be caused by the freeze-out process on to dust grains that affects these molecules or their main precursor molecules. For H^{13}CN , HN^{13}C , H^{13}CO^+ , the depletion sizes are found to be ~ 0.3 pc. In contrast, N_2H^+ and NH_3 appear to still be abundant in the SSN, which supports the selective freeze-out whereby molecules exhibit different behaviors when interacting with dust grains (e.g., Bergin & Tafalla 2007). Our results are roughly in line with the scenario that CO is the first to be depleted, followed by HCN, HNC, and HCNH^+ , while NH_3 and N_2H^+ are least affected. We also notice that even N_2H^+ abundances appear to drop toward the peak of the SSC when compared to ambient gas, which is similar to NH_3 (Friesen et al. 2016). Such low abundances indicate that even N_2H^+ and NH_3 begin to deplete from the gas phase in the SSC

(Bergin et al. 2002; Belloche & André 2004; Bergin & Tafalla 2007). Another potential scenario is that the elevated kinetic temperatures within the SSC lead to CO desorption back to the gas phase, facilitating the efficient destruction of N_2H^+ . This phenomenon would also trigger the desorption of NH_3 back to the gas phase, potentially enriching its abundances. However, the NH_3 abundance remains relatively low within the SSC, which might be attributed to the inefficient NH_3 desorption.

Figure 15 shows the pixel-by-pixel comparison of the abundances of HCNH^+ and the other five molecules. It is evident that H^{13}CO^+ , H^{13}CN , and HN^{13}C abundances generally increase with increasing HCNH^+ abundances toward SSN2, the SSC, bolo4, and bolo12. This can be readily explained by the freeze-out of CO, HCN, and HNC. However, we find that SSN1 exhibits the opposite trend where the H^{13}CO^+ , H^{13}CN , and HN^{13}C abundances generally decrease with increasing HCNH^+ abundances. Instead, HCNH^+ abundances are positively correlated with N_2H^+ and NH_3 in SSN1, in agreement with the spatially coincident distribution of HCNH^+ and N_2H^+ as shown

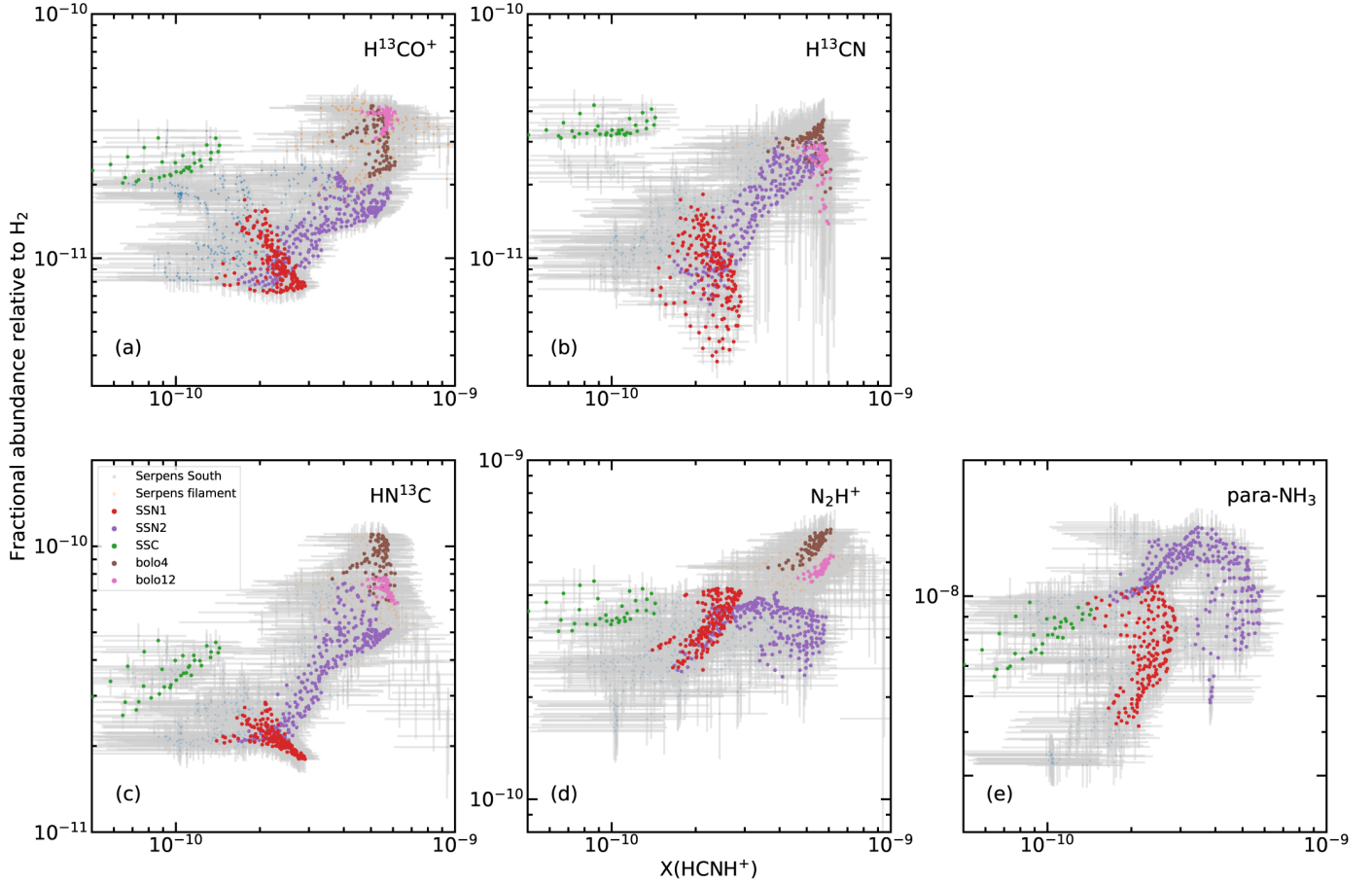


Fig. 15. Pixel-by-pixel comparison of the abundances of HCNH^+ and the other five molecules in the Serpens filament and Serpens South. The corresponding molecule is indicated in the upper-right corner of each panel. The subregions are indicated by the different colors in the legend of panel c.

in Fig. 14. This implies a different chemical formation pathway for HCNH^+ in SSN1 (details are discussed in Sect. 4.2). We also find that the SSC forms a distinct group in this figure, especially from the comparison of HCNH^+ with H^{13}CO^+ and H^{13}CN . The abundance ratios of $X(\text{HCNH}^+)/X(\text{H}^{13}\text{CO}^+)$ and $X(\text{HCNH}^+)/X(\text{H}^{13}\text{CN})$ are $\lesssim 5$ in the SSC, which are much lower than in other regions. This trend is similar to the results of Fontani et al. (2021) where warmer sources have lower $X(\text{HCNH}^+)/X(\text{HCO}^+)$ and $X(\text{HCNH}^+)/X(\text{HCN})$ ratios. This can be attributed to the elevated kinetic temperatures, which in turn enhance the H^{13}CO^+ and H^{13}CN abundances.

4. Discussion

4.1. Environmental dependence

As shown in Sect. 3.2, molecular abundances are sensitive to environmental conditions. Here, we attempt to quantify how the observed abundances depend on the physical parameters.

Figure 16 presents the comparison between the derived molecular abundances and H_2 column densities for the five molecules. In contrast to other molecules, the abundance of HCNH^+ shows an overall anticorrelation with H_2 column density with a strongly negative Pearson correlation coefficient of -0.73 . This further supports that HCNH^+ is abundant in low-density regions. It is also evident that the H^{13}CO^+ , H^{13}CN , HN^{13}C ,

and HCNH^+ abundances decrease with increasing H_2 column density toward the SSN. This pattern aligns with the depletion caused by the freeze-out process of CO , HCN , and HNC . Given that these molecules are known to be the main precursors of HCO^+ and HCNH^+ , the freeze-out process causes the depletion of HCO^+ and HCNH^+ . Interestingly, HCNH^+ has a lower abundance in the SSC than in the SSN. In contrast, HCO^+ and HCN are more abundant in the SSC than in the SSN, which could be potentially explained by the thermal desorption of CO , H_2O , and HCN from dust grains to the gas phase. Such desorption can be caused by elevated kinetic temperatures, for example due to outflow shocks. However, such a desorption process seems not to enhance the HCNH^+ abundance in the SSC.

In order to investigate the dependence of molecular abundances on gas kinetic temperature, we make use of the gas kinetic temperature derived from ammonia inversion transitions. Because of the lack of a gas kinetic temperature map toward the Serpens filament, we only investigate the molecular abundance variation as a function of the gas kinetic temperature toward Serpens South, which is shown in Fig. 17. Overall, the H^{13}CO^+ and H^{13}CN abundances increase with increasing kinetic temperatures, while that of HCNH^+ shows an opposite trend. HN^{13}C and N_2H^+ appear to be the least affected by variation in the kinetic temperature. Toward the SSC, H^{13}CO^+ , HN^{13}C , HCNH^+ , and N_2H^+ exhibit a different behavior from H^{13}CN whose molecular abundances appear to increase with increasing kinetic temperature. The different behaviors between H^{13}CN

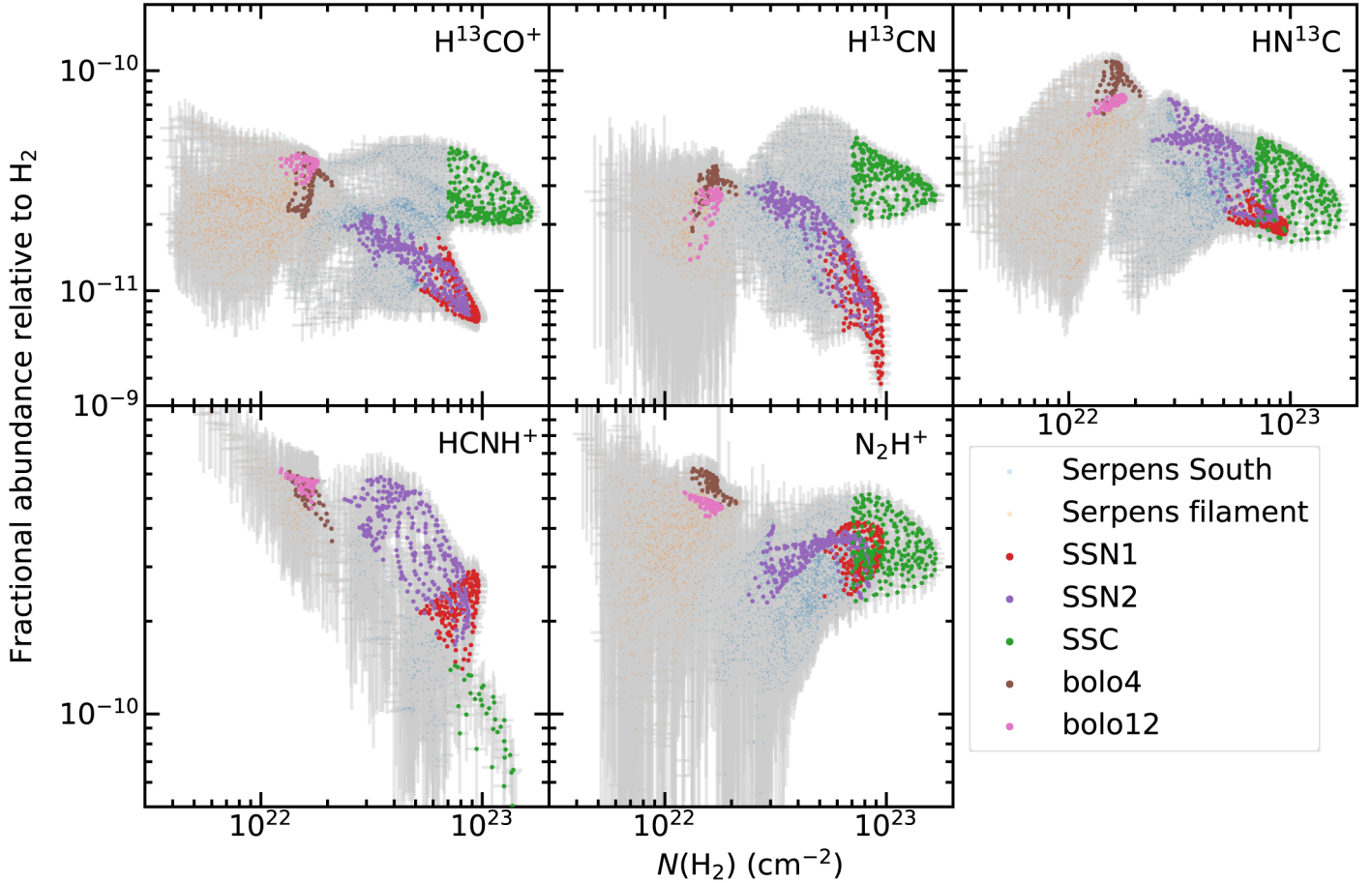


Fig. 16. Fractional abundances as a function of H_2 column density for the five molecules indicated in the top-right corner of each panel. Different regions are indicated by different colors, as shown in the legend.

and $HN^{13}C$ could be explained by the fact that HCN/HNC abundance ratio increases with kinetic temperature (e.g., Hacar et al. 2020). However, the gas kinetic temperature range (14–17 K) is too narrow to reach a more concrete conclusion.

4.2. Comparison between chemical models and observations

As shown in Sect. 4.1, the $HCNH^+$ abundance appears to be anticorrelated with the H_2 column density and kinetic temperature, which indicates that the $HCNH^+$ abundance deficit could be caused by the increased H_2 number density and kinetic temperature.

In order to test this hypothesis, we used the time-dependent gas-grain chemical code, *Chempl*¹¹ (Du 2021), to carry out astrochemical model calculations. The UMIST RATE12 chemical network¹² is adopted for this study (McElroy et al. 2013). Since HCN and HNC are important precursors of $HCNH^+$, their chemistry may also affect the chemistry of $HCNH^+$. Two reactions are believed to be important in the chemistry of HCN and HNC in molecular clouds (e.g., Schilke et al. 1992; Talbi et al. 1996; Graninger et al. 2014; Hacar et al. 2020):



¹¹ <https://github.com/fjdu/chempl>

¹² <http://udfa.ajmarkwick.net/>

Previous studies suggest that the assumption of an energy barrier, ΔE_{10} , of 200 K is suitable for reaction (10) (Graninger et al. 2014; Hacar et al. 2020), but quite different energy barriers $\Delta E_{11} = 20$ K (Hacar et al. 2020) and $\Delta E_{11} = 1125$ K (Graninger et al. 2014) have been proposed for reaction (11). Reaction (10) is included in the UMIST RATE12 chemical network, but the energy barrier is not up-to-date. On the other hand, reaction (11) is not included in the UMIST RATE12 chemical network. Hence, the two reactions with updated rate coefficients are augmented in the chemical network. The two different energy barriers of ΔE_{11} are used for comparison in the following.

Initial conditions are needed in the chemical code for the calculations. The initial elemental abundances are the same as in Table 3 of McElroy et al. (2013), which are based on diffuse cloud values. The interstellar radiation field, G_0 , is set to be $G_0 = 1$ in Habing units (Draine 1978). Although previous studies suggest that the abundances of HCN, HNC, and $HCNH^+$ can be regulated by the cosmic-ray ionization rate (CRIR; Fontani et al. 2021; Behrens et al. 2022), our measurements probe almost the same physical conditions and the CRIR is the same for all of the cloud volumes studied by us. Hence, we adopt the canonical value of $1.36 \times 10^{-17} \text{ s}^{-1}$ in dense molecular gas for the CRIR (e.g., van der Tak & van Dishoeck 2000). As shown in Figs. 1 and 2, the $HCNH^+$ emitting regions have kinetic temperatures ranging from 10 K to 20 K and H_2 column densities of $>1 \times 10^{22} \text{ cm}^{-2}$ (i.e., $A_v \gtrsim 10$ mag). We use two values from the kinetic temperature, 10 K and 20 K, to investigate the effects of the kinetic temperature variations. Given their high H_2 column

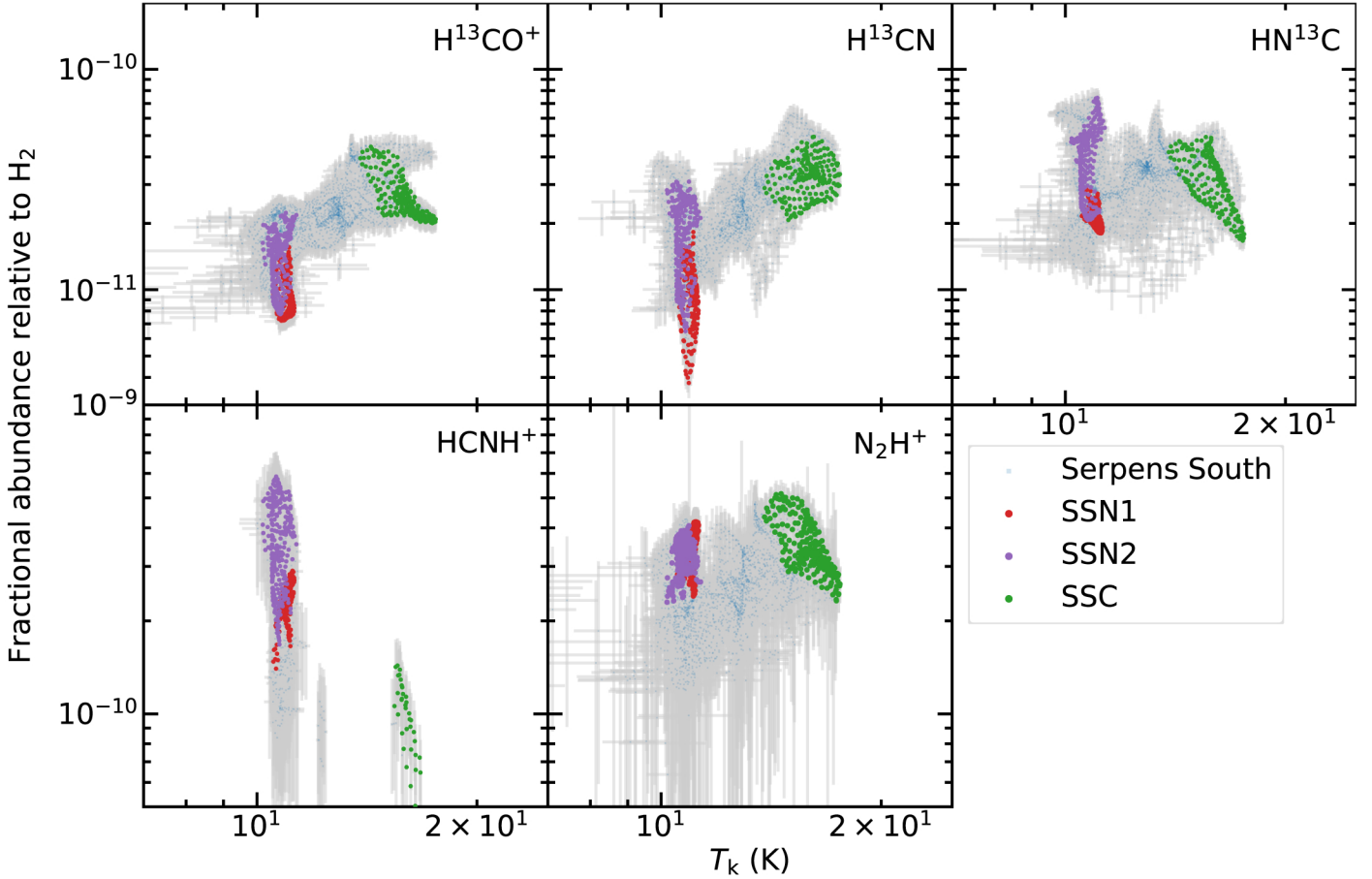


Fig. 17. Same as Fig. 16 but as a function of the gas kinetic temperature derived from ammonia inversion transitions.

densities, our target regions are well shielded from ultraviolet radiation. We used $A_v = 10$ mag as a fiducial case. The modeled H_2 number densities are in the range of 10^2 – 10^6 cm^{-3} .

In Fig. 18, we first compare the modeling results with $T_g = 10$ K and $T_g = 20$ K for a fixed H_2 number density of 10^4 cm^{-3} . These results suggest that the abundances change only slightly with gas temperature. This indicates that the HCNH^+ abundance does not significantly depend on the kinetic temperature in the range of 10–20 K. For HCNH^+ , the abundances are slightly higher for $T_g = 20$ K than for $T_g = 10$ K, which is different from Fig. 17. This is likely because the difference caused by gas temperature variation is negligible when compared to the impact of H_2 number densities. Hence, we mainly focus on the dependence of chemical abundances on the H_2 number density.

Figure 19 presents the time-dependent chemical modeling results of the abundances of HCNH^+ , H^{13}CN , HN^{13}C , H^{13}CO^+ , N_2H^+ and NH_3 , where a $^{12}\text{C}/^{13}\text{C}$ isotopic ratio of 70 is adopted to obtain the abundances of the ^{13}C -bearing molecules (e.g., Wilson & Rood 1994; Li et al. 2016; Yan et al. 2023) and the ortho-to-para ratio of NH_3 is assumed to 4.0 (see Fig. 3 in Takano et al. 2002, for instance). We find that the two different energy barriers for reaction (11) affect the results of HCNH^+ , H^{13}CN , and HN^{13}C . The general trend is that assuming an energy barrier $\Delta E_{11} = 1125$ K results in higher HCNH^+ , H^{13}CN , and HN^{13}C abundances than assuming $\Delta E_{11} = 20$ K. The HN^{13}C abundances are the most significantly affected. While our observed abundances can be roughly reproduced at an H_2 number density of 10^{3-4} cm^{-3} and cloud ages of around

10^{5-6} yr in Fig. 19, the high HN^{13}C abundances in TMC1 cannot be well reproduced by $\Delta E_{11} = 20$ K suggested by Hacar et al. (2020). This indicates that the rate coefficients derived with $\Delta E_{11} = 20$ K might not be suitable for the cold environments at $T_g \sim 10$ K. Therefore, we only use the results with $\Delta E_2 = 1125$ K suggested by Graninger et al. (2014) for the following discussions.

In Fig. 19, we also find that the HCNH^+ , H^{13}CN , and HN^{13}C abundances tend to reach the maximum earlier at higher H_2 densities and then decrease. The timescales to reach the maximum are nearly identical for the three molecules, regardless of the H_2 number densities, indicating that HCNH^+ abundances depend on the HCN and HNC abundances in the modeling results. Previous studies suggest that the reactions including Eqs. (3)–(6) are the main formation path of HCNH^+ (e.g., Loison et al. 2014a; Quénard et al. 2017; Fontani et al. 2021). HCN, HNC, H_2O , and HCO^+ are heavily depleted in cold and dense regions (see also Sect. 3.2). Since HCN and HNC are thought to be the main precursors of HCN^+ and HNC^+ (e.g., Loison et al. 2014a), these cations are also depleted in these regions. Similarly, H_2O serves as the precursor for H_3O^+ , which is also expected to be depleted under these conditions. If Eqs. (3)–(6) are the main formation pathways of HCNH^+ , this ion should also be depleted since its precursor molecules are heavily depleted. Therefore, the modeling results support that the decrease in its abundance is mainly caused by the freeze-out process, and the timescale of the abundance peak at a given H_2 number density can be readily explained by the depletion timescale that

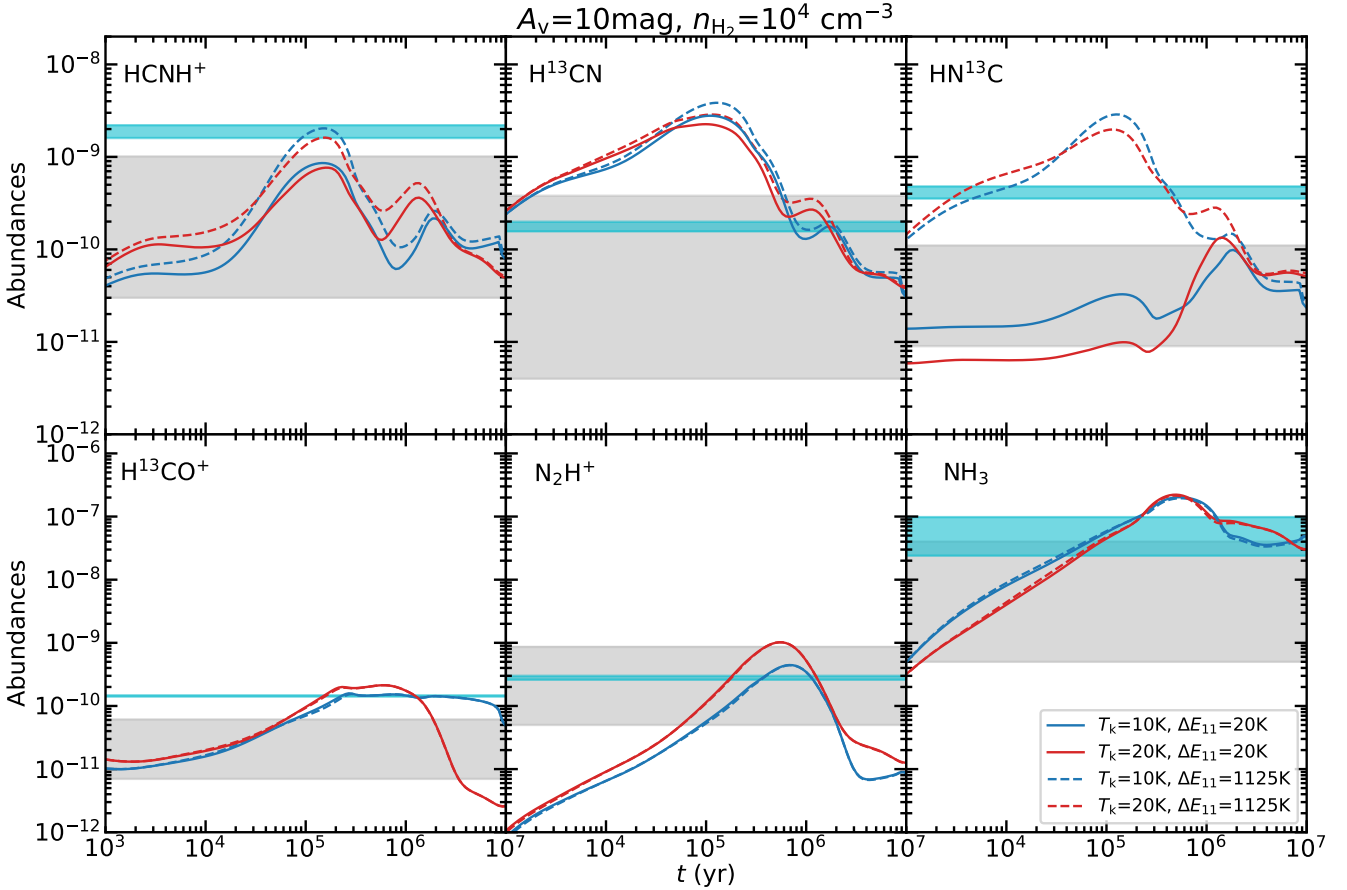


Fig. 18. Molecular abundances relative to H_2 as a function of time, estimated from *Chempl* (Du 2021). The different colors correspond to different kinetic temperatures. The solid and dashed lines represent the modeling results with the energy barrier $\Delta E_{11} = 20$ K and $\Delta E_{11} = 1125$ K for reaction (11), respectively. The observed molecular abundances in our studies are indicated by the gray shaded regions, while the molecular abundances in TMC1 (Agúndez & Wakelam 2013) are indicated by the cyan shaded regions. The other physical conditions are indicated at the top of this figure.

inversely depends on the H_2 number density (e.g., Caselli et al. 1999). Figure 20 presents the modeled abundances of HCNH^+ , HCN , HNC , HCO^+ , N_2H^+ and NH_3 as a function of H_2 number density at a simulated timescale of 10^6 yr. This demonstrates the anticorrelation between the H_2 number density and molecular abundances, which readily explains the observed HCNH^+ abundance dependence of H_2 column density in Fig. 16. These results suggest that HCNH^+ should be the most abundant in low-density regions where precursor species like HCN and HNC do not freeze out onto dust grains. Figure 21 presents the molecular abundances reproduced by *Chempl* as a function of simulation times for the same physical conditions (i.e., $T_g=10$ K, $n_{\text{H}_2} = 10^4 \text{ cm}^{-3}$). This figure supports the selective freeze-out scenario in which HCN and HNC deplete earlier than N_2H^+ and NH_3 .

The modeling results are consistent with the observational finding that HCNH^+ is the most abundant in starless cores in their early evolutionary phase. Since the density is expected to increase during gravitational collapse, HCNH^+ abundances should decrease after the onset of infall. This also explains why the starless core TMC1 has a much higher HCNH^+ abundance than the prestellar core L1544 and our observed regions (see Fig. 11). Investigation of HCNH^+ in different evolutionary stages of low-mass star formation (see Fig. 12 and Appendix B) and non-detection of HCNH^+ (3–2) around class 0 protostars (Belloche et al. 2020) are also in line with this scenario. On

the other hand, mass accretion flows in the SSN are indicated by previous observations (e.g., Friesen et al. 2013). Hence, we suggest that the HCNH^+ abundance gradient along the SSN2 in Fig. 14a can be a result of the longitudinal mass accretion.

Although HCNH^+ depletion is indeed found and appears to correlate with HCN and HNC depletion in Sect. 3.2 and Sect. 4.1, the HCNH^+ abundances in SSN1 show an anticorrelation with HCN and HNC , and a positive correlation with N_2H^+ and NH_3 . Moreover, the HCNH^+ emission peak coincides with N_2H^+ emission toward SSN1. These facts imply that HCNH^+ does not follow the depletion of HCN and HNC in SSN1. Such trends cannot be explained by our chemical modeling results (see Figs. 19 and 20). This suggests additional HCNH^+ formation paths from molecules that do not freeze out. Because species like NH_3 and N_2 can still survive in the gas phase even when HCN and HNC are heavily depleted, we suggest that the ion-neutral reactions from these species become more important in the formation of HCNH^+ toward freeze-out regions.

In order to further study the importance of the formation pathways for HCNH^+ , we compare the rates of reactions (1)–(7). For a binary reaction, the reaction rate is defined as $v_{\text{rate}} = kX_A X_B$, where k is the reaction rate coefficient, and X_A and X_B are the abundances of the two reactants. However, the rate coefficients of reactions (1), (2) and (7) are not available in the RATE12 chemical network (McElroy et al. 2013). The rate

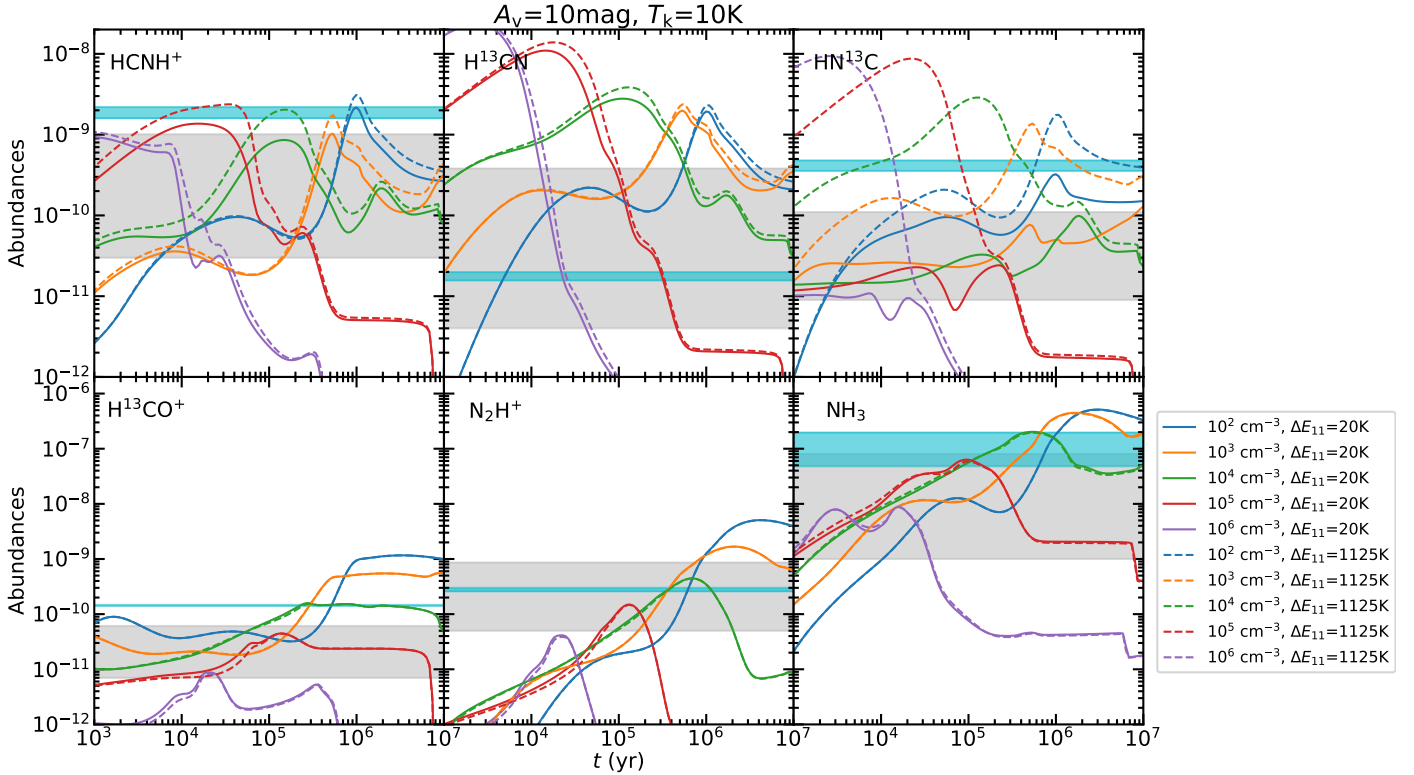


Fig. 19. Molecular abundances relative to H_2 as a function of time, estimated from *Chempl* (Du 2021). The different colors correspond to the different H_2 number densities, from 10^2 cm^{-3} to 10^6 cm^{-3} . The solid and dashed lines represent the modeling results with the energy barrier $\Delta E_{11} = 20 \text{ K}$ and $\Delta E_{11} = 1125 \text{ K}$ for reaction (11), respectively. The observed molecular abundances in our studies are indicated by the gray shaded regions, while the molecular abundances in TMC1 (Agúndez & Wakelam 2013) are indicated by the cyan shaded regions.

coefficients at 300 K were suggested to be $1.7 \times 10^{-9} \text{ cm}^3 \text{ s}^{-1}$ and $7 \times 10^{-11} \text{ cm}^3 \text{ s}^{-1}$ for reactions (1) and (2), respectively (Schilke et al. 1991). In the RATE12 chemical network, the same paths to form its isomer H_2NC^+ exist with the rate coefficients of $1.5 \times 10^{-9} \text{ cm}^3 \text{ s}^{-1}$ and $6.7 \times 10^{-11} \text{ cm}^3 \text{ s}^{-1}$ at 10 K (Smith & Adams 1977; Fehsenfeld 1976). The rate coefficient of reaction (1) agrees with the latest calculations within uncertainties (Martinez et al. 2008). Hence, these values are comparable to the values of Schilke et al. (1991). This would be expected if the branching ratios of reactions to form $HCNH^+$ and H_2NC^+ are identical. Hence, we simply take these two values for reactions (1) and (2). Based on previous studies, the rate coefficient of reaction (7) is $9 \times 10^{-10} \text{ cm}^3 \text{ s}^{-1}$ at 10 K (Knight et al. 1988; Loison et al. 2014b). These values are thus used for the qualitative calculations.

Based on our chemical modeling results and the rate coefficients discussed above, we can estimate the rates of reactions (1)–(7) to assess the relative importance of these formation paths as a function of time. Because reactions (1), (2), and (7) are not included in our modeling calculations, we only took the molecular abundances from the modeling results to estimate the formation rates. Figure 22 presents the comparison of the reaction rates for the chemical model using a number density of 10^4 cm^{-3} . We surprisingly find that reaction (7) involving the hydrogenation of C_2N^+ emerges as the dominant formation pathway for $HCNH^+$, superseding all other competing reactions by several orders of magnitude. We investigate the modeling results with an updated chemical network augmented with reaction (7) in Appendix C, which suggests that reaction (7) can make significant contributions to the formation of $HCNH^+$ at least on simulated timescales of $< 10^5 \text{ yr}$. This further casts doubts on the

main formation path of $HCNH^+$ via reactions (1)–(6). Furthermore, reaction (2) is as efficient as reactions (5)–(6) at timescales on the order of $\lesssim 10^5 \text{ yr}$. On the other hand, reaction (1) is relatively less efficient, but becomes non-negligible at a timescale of $\sim 10^6 \text{ yr}$ when compared with reactions (2)–(6). The significance of missing reactions, particularly reaction (7), in the formation of $HCNH^+$ is underscored by this comparison. More complete chemical networks and laboratory efforts to derive accurate rate coefficients will help improve our understanding of the chemistry of $HCNH^+$ and eventually larger nitrogen-bearing molecules.

4.3. Collisional excitation

Owing to its small dipole moment (0.29 D; Botschwina 1986), the low J transitions of $HCNH^+$ have Einstein A coefficients of $< 5 \times 10^{-6} \text{ s}^{-1}$ (see Table 1), which are an order of magnitude lower than those of the other molecular transitions used in this work. By utilizing the latest rate coefficients governing collisions with H_2^{13} (C. Bop, priv. comm.) and Eq. (4) in Shirley (2015), we calculated the optically thin critical densities of $HCNH^+$ (1–0), (2–1), (3–2) at 10 K to be $2.0 \times 10^2 \text{ cm}^{-2}$, $1.7 \times 10^3 \text{ cm}^{-2}$, and $5.2 \times 10^3 \text{ cm}^{-2}$, respectively. Intriguingly, these critical densities are even lower than the corresponding low- J CO critical densities in the optically thin regime (Yang et al. 2010), implying

¹³ The adopted collisional rate coefficients are more accurate than those presented in Bop & Lique (2023) because the $j=2$ excited energy level of H_2 has been taken into account in the latest results (C. Bop, priv. comm.).

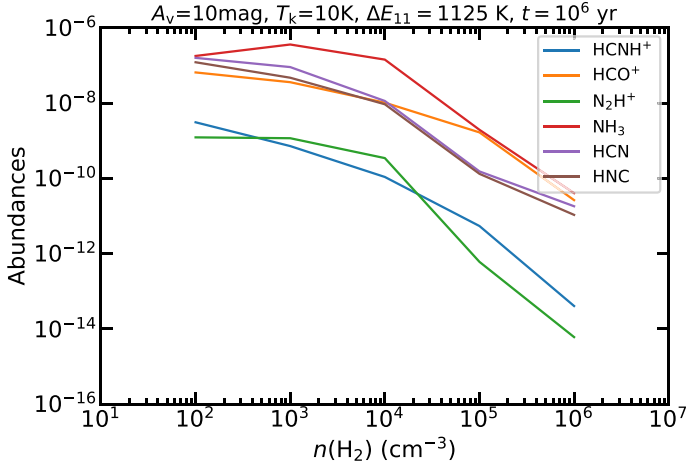


Fig. 20. Molecular abundances of HCNH⁺, HCN, HNC, HCO⁺, N₂H⁺, and NH₃ as a function of H₂ number density on a simulated timescale of 10⁶ yr. The adopted physical conditions are indicated at the top of this figure.

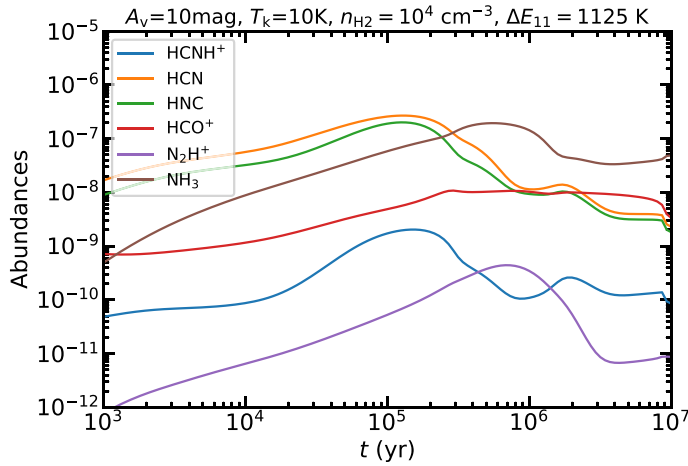


Fig. 21. Temporal evolution of the abundances of HCNH⁺, HCN, HNC, HCO⁺, N₂H⁺, and NH₃, estimated from *Chempl* (Du 2021). The adopted physical conditions are indicated at the top of this figure.

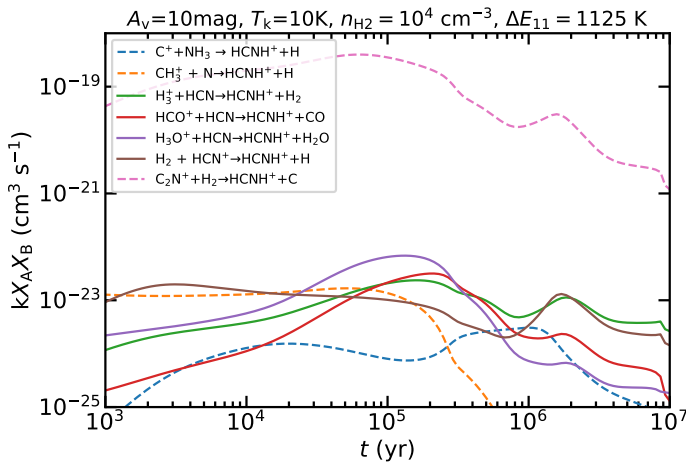


Fig. 22. Reaction rates of the different formation paths of HCNH⁺ as a function of time. The solid lines indicate reactions that are included in the RATE12 chemical network, whereas the dashed lines include potentially important reactions not incorporated in the network.

that the energy levels connecting these HCNH⁺ transitions in LTE and can trace low-density regions. Therefore, we argue that HCNH⁺ can be regarded as a good probe of pristine molecular gas prior to the onset of gravitational collapse.

Recent studies have suggested that electrons may play a significant role in the excitation of molecular tracers like HCN and CH in molecular clouds (Goldsmith & Kauffmann 2017; Jacob et al. 2021). Adopting the same approximation that the collisional cross sections for electron excitation will be dominated by long-range forces and scale as the square of the permanent electric dipole moment (Goldsmith & Kauffmann 2017), we can derive the HCNH⁺-e⁻ collisional rates by scaling the values of the HCN-e⁻ and CH⁺-e⁻ collisional rates from Faure et al. (2007, 2017). Because the dipole moment (0.29 D) of HCNH⁺ is about 0.10 and 0.17 times those of HCN (2.985 D; Ebenstein & Muentner 1984) and CH⁺ (1.683 D; Cheng et al. 2007), the HCNH⁺-e⁻ collisional rates are found to be $\sim 2 \times 10^{-13}$ cm³ s⁻¹ and $\sim 1 \times 10^{-12}$ cm³ s⁻¹, respectively. Utilizing these values, we can estimate the critical electron fractional abundance that is required to make the electron collision rate equal to the H₂ collision rate, $x^*(e^-) = n_c(e^-)/n_c(H_2)$ (Goldsmith & Kauffmann 2017). $x^*(e^-)$ is found to be $\sim (1 - 4) \times 10^{-3}$, which is considerably greater than the expected electron abundances of a few times 10⁻⁹ in molecular clouds (Caselli et al. 2002b). On the other hand, molecular clouds with H₂ number densities of $\geq 5 \times 10^3$ cm⁻³ are sufficient to thermalize the excitation temperatures due to the low critical H₂ densities of the three low *J* HCNH⁺ transitions. Therefore, we conclude that electron collisions with HCNH⁺ are unlikely to be significant in molecular clouds. We also note that the approximation of $x^*(e^-)$ is very crude especially in the case of ion-electron interactions, because the dipole moment is no longer the only dominant term in the long-range forces.

5. Summary and outlook

Using the IRAM 30 m and APEX 12 m telescopes, we have mapped HCNH⁺, H¹³CN, HN¹³C, H¹³CO⁺, and N₂H⁺ transitions toward the Serpens filament and Serpens South. Our primary findings are summarized below:

1. Our observations of the two regions provide the first reliable distributions of HCNH⁺, which suggest that HCNH⁺ is abundant in cold and quiescent regions but shows a deficit toward star-forming regions (i.e., emb10 and the SSC).
2. An LTE analysis suggests that the observed HCNH⁺ column densities range from 4.2×10^{12} cm⁻² to 2.7×10^{13} cm⁻², which leads to its corresponding abundance relative to H₂ ranging from 3.1×10^{-11} in protostellar cores to 5.9×10^{-10} in prestellar cores. HCNH⁺ is more abundant in molecular cores prior to gravitational collapse than in prestellar and star-forming cores. This result is in agreement with the scenario that HCNH⁺ abundances decrease as the region evolves.
3. Based on our observations, we find that HCNH⁺ abundances generally decrease with increasing H₂ column density. We suggest that HCNH⁺ destruction in cold environments (*T_g* ~ 10 K) mainly depends on the increased H₂ number density, which causes the freeze-out of its precursors HCN and HNC.
4. Current astrochemical models cannot explain the observed trend in SSN1, where the HCNH⁺ abundance shows an anticorrelation with HCN and HNC but a positive correlation with N₂H⁺ and NH₃. This indicates that additional

formation paths of HCNH^+ from molecules (e.g., N_2 and NH_3) that do not freeze out should play an important role in the formation of HCNH^+ in the freeze-out regions where HCN and HNC are heavily depleted.

- Comparing the reaction rates of possible formation paths of HCNH^+ , we find that important chemical reactions for the formation of HCNH^+ are likely missing in the RATE12 chemical network. More complete chemical networks and accurate rate coefficients are indispensable to understand the chemistry of HCNH^+ .
- The optically thin critical densities for HCNH^+ (1–0), (2–1), and (3–2) at 10 K, resulting from collisions with H_2 molecules, are found to be $2.0 \times 10^2 \text{ cm}^{-2}$, $1.7 \times 10^3 \text{ cm}^{-2}$, and $5.2 \times 10^3 \text{ cm}^{-2}$, respectively. These values suggest that LTE for these transitions should be readily achieved in molecular clouds. Since LTE is a good approximation for HCNH^+ , the derived HCNH^+ column densities should be reliable (see Table 3). On the other hand, electron excitation plays a negligible role in these transitions in molecular clouds.

Our observations have shown that HCNH^+ appears to become deficient after the onset of gravitational collapse in low-mass star formation regions (see also Appendix B). However, the observational picture toward other environments is still elusive. Although HCNH^+ has already been detected in a number of high-mass star formation regions (e.g., Fontani et al. 2021), the influence of the environment on its spatial distribution is not well investigated in such environments. We also searched for information on HCNH^+ in previous line surveys of the circumstellar envelopes of evolved stars. HCNH^+ (2–1) has been observed in the 2 mm line survey of the asymptotic giant branch star IRC+10216 (Cernicharo et al. 2000; He et al. 2008), and HCNH^+ (3–2) has been covered in the 1 mm line survey of IRC+10216 and the red supergiant VY CMa (Tenenbaum et al. 2010; Kamiński et al. 2013), but the HCNH^+ transitions were not detected by these sensitive surveys. This indicates that this molecular ion might not be abundant in circumstellar envelopes of evolved stars. Regarding extragalactic observations, this molecule appears to be tentatively detected in NGC 4945 (Villicañá-Pedraza et al. 2016, 2017).

Acknowledgments. We acknowledge the IRAM 30 m and APEX 12 m staff for their assistance with our observations. Y.G. is grateful to Ashly Sebastine for her preliminary investigation of the APEX 12 m pointed observations toward Serpens South. Fujun Du is supported by the National Natural Science Foundation of China (NSFC) through grants 12041305 and 11873094. C.H. has been funded by Chinese Academy of Sciences President's International Fellowship Initiative under Grant No. 2022VMA0018. A.M.J. acknowledges support by USRA through a grant for SOFIA Program 08-0038. X.D.T. acknowledges the support of the Natural Science Foundation of Xinjiang Uygur Autonomous Region under Grant No. 2022D01E06, the Tianshan Talent Program of Xinjiang Uygur Autonomous Region under Grant No. 2022TSYCLJ0005, and the Chinese Academy of Sciences “Light of West China” Program under Grant No. xbzg-zdsys-202212. C. Bop acknowledges financial support from the European Research Council (Consolidator Grant COLLEXISM, Grant Agreement No. 811363). M.R.R. is a Jansky Fellow of the National Radio Astronomy Observatory, USA. The research leading to these results has received funding from the European Union's Horizon 2020 research and innovation program under grant agreement No 101004719 [Opticon RadioNet Pilot ORP]. This publication is based on data acquired with the Atacama Pathfinder Experiment (APEX). APEX is a collaboration between the Max-Planck-Institut für Radioastronomie, the European Southern Observatory, and the Onsala Space Observatory. This research has made use of NASA's Astrophysics Data System. This work also made use of Python libraries including Astropy (<https://www.astropy.org/>; Astropy Collaboration 2013), NumPy (<https://www.numpy.org/>; van der Walt et al. 2011), SciPy (<https://www.scipy.org/>; Jones et al. 2001), Matplotlib (<https://matplotlib.org/>; Hunter 2007), APLpy (Robitaille & Bressert 2012), and seaborn (<https://seaborn.pydata.org/>; Waskom 2021). We would like to thank the anonymous referee for helpful comments.

References

- Aalto, S., Polatidis, A. G., Hüttemeister, S., & Curran, S. J. 2002, *A&A*, 381, 783
 Agúndez, M., & Wakelam, V. 2013, *Chem. Rev.*, 113, 8710
 André, P., Men'shchikov, A., Bontemps, S., et al. 2010, *A&A*, 518, L102
 Astropy Collaboration (Robitaille, T. P., et al.) 2013, *A&A*, 558, A33
 Behrens, E., Mangum, J. G., Holdship, J., et al. 2022, *ApJ*, 939, 119
 Belloche, A., & André, P. 2004, *A&A*, 419, L35
 Belloche, A., Maury, A. J., Maret, S., et al. 2020, *A&A*, 635, A198
 Bergin, E. A., & Tafalla, M. 2007, *ARA&A*, 45, 339
 Bergin, E. A., Alves, J., Huard, T., & Lada, C. J. 2002, *ApJ*, 570, L101
 Bop, C. T., & Lique, F. 2023, *J. Chem. Phys.*, 158, 074304
 Botschwina, P. 1986, *Chem. Phys. Lett.*, 124, 382
 Burkhardt, A. M., Loomis, R. A., Shingledecker, C. N., et al. 2021, *Nat. Astron.*, 5, 181
 Carter, M., Lazareff, B., Maier, D., et al. 2012, *A&A*, 538, A89
 Caselli, P., Walmsley, C. M., Tafalla, M., Dore, L., & Myers, P. C. 1999, *ApJ*, 523, L165
 Caselli, P., Benson, P. J., Myers, P. C., & Tafalla, M. 2002a, *ApJ*, 572, 238
 Caselli, P., Walmsley, C. M., Zucconi, A., et al. 2002b, *ApJ*, 565, 344
 Cernicharo, J., Castets, A., Duvert, G., & Guilloteau, S. 1984, *A&A*, 139, L13
 Cernicharo, J., Guélin, M., & Kahane, C. 2000, *A&AS*, 142, 181
 Cheng, M., Brown, J. M., Rosmus, P., et al. 2007, *Phys. Rev. A*, 75, 012502
 Cravens, T. E., Robertson, I. P., Waite, J. H., et al. 2006, *Geophys. Res. Lett.*, 33, L07105
 Draine, B. T. 1978, *ApJS*, 36, 595
 Du, F. 2021, *Res. Astron. Astrophys.*, 21, 077
 Dzib, S., Loinard, L., Mioduszewski, A. J., et al. 2010, *ApJ*, 718, 610
 Ebenstein, W. L., & Muentzer, J. S. 1984, *J. Chem. Phys.*, 80, 3989
 Endres, C. P., Schlemmer, S., Schilke, P., Stutzki, J., & Müller, H. S. P. 2016, *J. Mol. Spectrosc.*, 327, 95
 Enoch, M. L., Glenn, J., Evans, II, N. J., et al. 2007, *ApJ*, 666, 982
 Enoch, M. L., Evans, Neal J., I., Sargent, A. I., & Glenn, J. 2009, *ApJ*, 692, 973
 Faure, A., Varambhia, H. N., Stoecklin, T., & Tennyson, J. 2007, *MNRAS*, 382, 840
 Faure, A., Halvick, P., Stoecklin, T., et al. 2017, *MNRAS*, 469, 612
 Fehsenfeld, F. C. 1976, *ApJ*, 209, 638
 Fiorellino, E., Elia, D., André, P., et al. 2021, *MNRAS*, 500, 4257
 Fixsen, D. J. 2009, *ApJ*, 707, 916
 Fontani, F., Colzi, L., Redaelli, E., Sipilä, O., & Caselli, P. 2021, *A&A*, 651, A94
 Friesen, R. K., Medeiros, L., Schnee, S., et al. 2013, *MNRAS*, 436, 1513
 Friesen, R. K., Bourke, T. L., Di Francesco, J., Gutermuth, R., & Myers, P. C. 2016, *ApJ*, 833, 204
 Ginsburg, A., & Mirocha, J. 2011, Astrophysics Source Code Library [[record ascl:1109.0001](https://ui.adsabs.org/record/1109.0001)]
 Glenn, J., Ade, P. A. R., Amarie, M., et al. 2003, *SPIE Conf. Ser.*, 4855, 30
 Goicoechea, J. R., Lique, F., & Santa-Maria, M. G. 2022, *A&A*, 658, A28
 Goldsmith, P. F., & Kauffmann, J. 2017, *ApJ*, 841, 25
 Gong, Y., Li, G. X., Mao, R. Q., et al. 2018, *A&A*, 620, A62
 Gong, Y., Belloche, A., Du, F. J., et al. 2021, *A&A*, 646, A170
 Gong, Y., Belloche, A., Du, F. J., et al. 2023, *A&A*, 672, C1
 Graninger, D. M., Herbst, E., Öberg, K. I., & Vasyunin, A. I. 2014, *ApJ*, 787, 74
 Güsten, R., Nyman, L. Å., Schilke, P., et al. 2006, *A&A*, 454, L13
 Gutermuth, R. A., Bourke, T. L., Allen, L. E., et al. 2008, *ApJ*, 673, L151
 Hacar, A., Bosman, A. D., & van Dishoeck, E. F. 2020, *A&A*, 635, A4
 He, J. H., Dinh-V-Trung, Kwok, S., et al. 2008, *ApJS*, 177, 275
 Herbst, E. 1978, *ApJ*, 222, 508
 Herbst, E., & Klemperer, W. 1973, *ApJ*, 185, 505
 Herbst, E., Terzieva, R., & Talbi, D. 2000, *MNRAS*, 311, 869
 Hezareh, T., Houde, M., McCoey, C., Vastel, C., & Peng, R. 2008, *ApJ*, 684, 1221
 Hirota, T., Yamamoto, S., Mikami, H., & Ohishi, M. 1998, *ApJ*, 503, 717
 Hunter, J. D. 2007, *Comput. Sci. Eng.*, 9, 90
 Jacob, A. M., Menten, K. M., Wiesemeyer, H., & Ortiz-León, G. N. 2021, *A&A*, 650, A133
 Jin, M., Lee, J.-E., & Kim, K.-T. 2015, *ApJS*, 219, 2
 Jones, E., Oliphant, T., Peterson, P., et al. 2001, *SciPy: Open source scientific tools for Python*
 Jørgensen, J. K., Belloche, A., & Garrod, R. T. 2020, *ARA&A*, 58, 727
 Kamiński, T., Gottlieb, C. A., Menten, K. M., et al. 2013, *A&A*, 551, A113
 Kerkeni, B., & Simmie, J. M. 2023, *J. Phys. Chem. A*, 127, 5382
 Kirk, H., Myers, P. C., Bourke, T. L., et al. 2013, *ApJ*, 766, 115
 Klein, B., Hochgürtel, S., Krämer, I., et al. 2012, *A&A*, 542, A3
 Knight, J. S., Petrie, S. A. H., Freeman, C. G., et al. 1988, *J. Am. Chem. Soc.*, 110, 5286
 Könyves, V., André, P., Men'shchikov, A., et al. 2015, *A&A*, 584, A91
 Lefloch, B., Bachiller, R., Ceccarelli, C., et al. 2018, *MNRAS*, 477, 4792
 Levshakov, S. A., Henkel, C., Reimers, D., et al. 2013, *A&A*, 553, A58

- Levshakov, S. A., Henkel, C., Reimers, D., & Wang, M. 2014, *A&A*, 567, A78
- Li, J., Shen, Z.-Q., Wang, J., et al. 2016, *ApJ*, 824, 136
- Loison, J.-C., Wakelam, V., & Hickson, K. M. 2014a, *MNRAS*, 443, 398
- Loison, J.-C., Wakelam, V., Hickson, K. M., Bergeat, A., & Mereau, R. 2014b, *MNRAS*, 437, 930
- Loughnane, R. M., Redman, M. P., Thompson, M. A., et al. 2012, *MNRAS*, 420, 1367
- Mangum, J. G., & Shirley, Y. L. 2016, *PASP*, 128, 029201
- Martinez, Oscar, J., Betts, N. B., Villano, S. M., et al. 2008, *ApJ*, 686, 1486
- Maury, A. J., André, P., Men'shchikov, A., Könyves, V., & Bontemps, S. 2011, *A&A*, 535, A77
- McElroy, D., Walsh, C., Markwick, A. J., et al. 2013, *A&A*, 550, A36
- Mendes, M. B., Buhr, H., Berg, M. H., et al. 2012, *ApJ*, 746, L8
- Mottram, J. C., van Dishoeck, E. F., Kristensen, L. E., et al. 2017, *A&A*, 600, A99
- Mouschovias, T. C., & Ciolek, G. E. 1999, in *NATO Advanced Study Institute (ASI) Series C*, 540, The Origin of Stars and Planetary Systems, ed. C. J. Lada, & N. D. Kylafis, 305
- Muders, D., Hafok, H., Wyrowski, F., et al. 2006, *A&A*, 454, L25
- Nakamura, F., Sugitani, K., Shimajiri, Y., et al. 2011, *ApJ*, 737, 56
- Nakamura, F., Sugitani, K., Tanaka, T., et al. 2014, *ApJ*, 791, L23
- Ortiz-León, G. N., Dzib, S. A., Kounkel, M. A., et al. 2017, *ApJ*, 834, 143
- Ortiz-León, G. N., Loinard, L., Dzib, S. A., et al. 2018, *ApJ*, 869, L33
- Ortiz-León, G. N., Plunkett, A. L., Loinard, L., et al. 2021, *AJ*, 162, 68
- Ortiz-León, G. N., Dzib, S. A., Loinard, L., et al. 2023, *A&A*, 673, A1
- Pacheco-Vázquez, S., Fuente, A., Agúndez, M., et al. 2015, *A&A*, 578, A81
- Pety, J. 2005, in *SF2A-2005: Semaine de l'Astrophysique Française*, eds. F. Casoli, T. Contini, J. M. Hameury, & L. Pagani, 721
- Plunkett, A. L., Arce, H. G., Corder, S. A., et al. 2015a, *ApJ*, 803, 22
- Plunkett, A. L., Arce, H. G., Mardones, D., et al. 2015b, *Nature*, 527, 70
- Pratap, P., Dickens, J. E., Snell, R. L., et al. 1997, *ApJ*, 486, 862
- Quénard, D., Vastel, C., Ceccarelli, C., et al. 2017, *MNRAS*, 470, 3194
- Robitaille, T., & Bressert, E. 2012, *Astrophysics Source Code Library* [[record ascl:1208.017](https://www.ascl.net/record/1208.017)]
- Schilke, P., Walmsley, C. M., Millar, T. J., & Henkel, C. 1991, *A&A*, 247, 487
- Schilke, P., Walmsley, C. M., Pineau Des Forets, G., et al. 1992, *A&A*, 256, 595
- Shiba, Y., Hirano, T., Nagashima, U., & Ishii, K. 1998, *J. Chem. Phys.*, 108, 698
- Shirley, Y. L. 2015, *PASP*, 127, 299
- Smith, D., & Adams, N. G. 1977, *Chem. Phys. Lett.*, 47, 145
- Sun, J., Guterma, R. A., Wang, H., et al. 2022, *MNRAS*, 516, 5244
- Takano, S., Nakai, N., & Kawaguchi, K. 2002, *PASJ*, 54, 195
- Talbi, D., Ellinger, Y., & Herbst, E. 1996, *A&A*, 314, 688
- Tanaka, T., Nakamura, F., Awazu, Y., et al. 2013, *ApJ*, 778, 34
- Tenenbaum, E. D., Dodd, J. L., Milam, S. N., Woolf, N. J., & Ziurys, L. M. 2010, *ApJS*, 190, 348
- Toelle, F., Ungerechts, H., Walmsley, C. M., Winnewisser, G., & Churchwell, E. 1981, *A&A*, 95, 143
- Tritsis, A., Basu, S., & Federrath, C. 2023, *MNRAS*, 521, 5087
- Turner, B. E., Amano, T., & Feldman, P. A. 1990, *ApJ*, 349, 376
- Ulich, B. L., & Haas, R. W. 1976, *ApJS*, 30, 247
- van der Tak, F. F. S. & van Dishoeck, E. F. 2000, *A&A*, 358, A79
- van der Walt, S., Colbert, S. C., & Varoquaux, G. 2011, *Comput. Sci. Eng.*, 13, 22
- Villicaña-Pedraza, I., Guesten, R., Armijos Abendaño, J., et al. 2016, in *41st COSPAR Scientific Assembly*, 41, F3.1-27-16
- Villicaña-Pedraza, I., Martín, S., Martín-Pintado, J., et al. 2017, in *Formation and Evolution of Galaxy Outskirts*, 321, eds. A. Gil de Paz, J. H. Knapen, & J. C. Lee, 305
- Walmsley, C. M., Churchwell, E., Nash, A., & Fitzpatrick, E. 1982, *ApJ*, 258, L75
- Waskom, M. L. 2021, *J. Open Source Softw.*, 6, 3021
- Wilson, T. L., & Rood, R. 1994, *ARA&A*, 32, 191
- Yan, Y. T., Henkel, C., Kobayashi, C., et al. 2023, *A&A*, 670, A98
- Yang, B., Stancil, P. C., Balakrishnan, N., & Forrey, R. C. 2010, *ApJ*, 718, 1062
- Zhang, M., Fang, M., Wang, H., et al. 2015, *ApJS*, 219, 21
- Ziurys, L. M., & Turner, B. E. 1986, *ApJ*, 302, L31
- Ziurys, L. M., Apponi, A. J., & Yoder, J. T. 1992, *ApJ*, 397, L123
- Ziurys, L. M., Savage, C., Brewster, M. A., et al. 1999, *ApJ*, 527, L67
- Zucker, C., Speagle, J. S., Schlafly, E. F., et al. 2019, *ApJ*, 879, 125

Appendix A: Molecular column density maps

We present the column density maps of H^{13}CN , HN^{13}C , H^{13}CO^+ , and HCNH^+ in Figs. A.1–A.2.

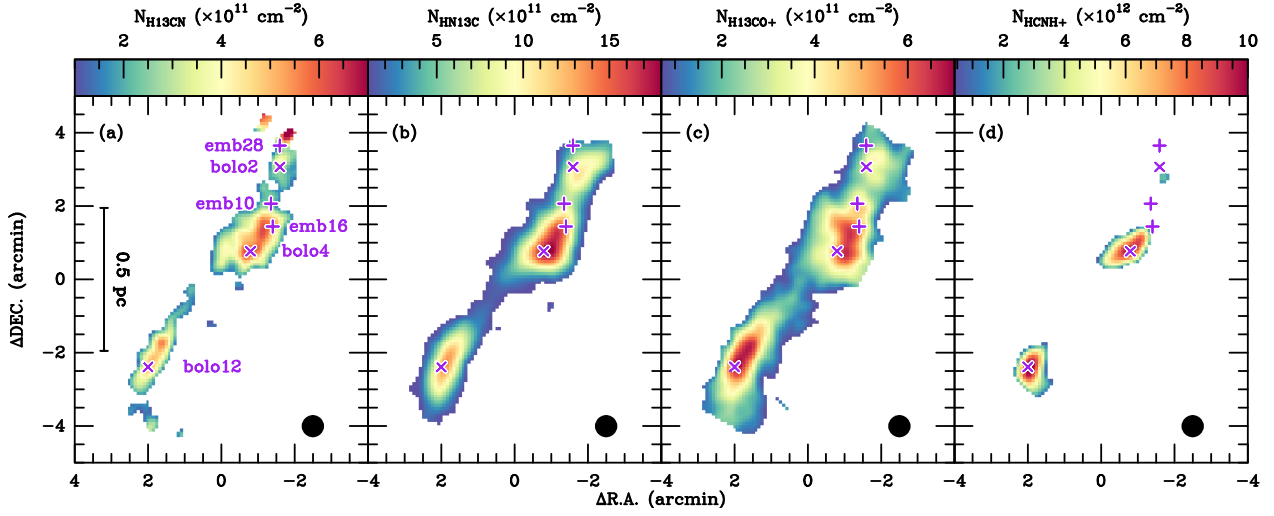


Fig. A.1. Molecular column density maps of the Serpens filament. The markers are the same as in Fig. 1.

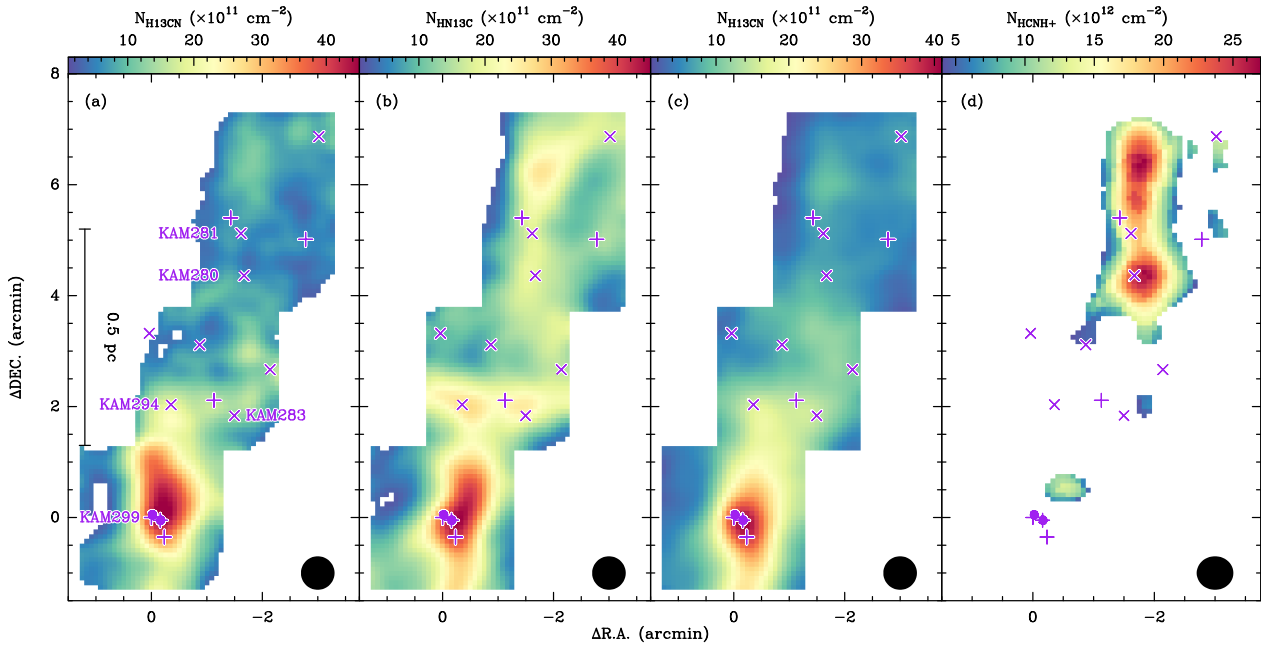


Fig. A.2. Molecular column density maps of Serpens South. The markers are the same as in Fig. 2.

Appendix B: HCNH^+ in different evolutionary stages of low-mass star formation

Figure B.1 shows the HCNH^+ spectra of low-mass star-formation regions in different environments. The HCNH^+ spectra of TMC1, L1527, IRAS4A, L1157-mm, L1157-B1, SVS 13A, and L1448-R2 are based on IRAM 30 m observations, and the data are directly taken from the Large Program “Astrochemical Surveys At IRAM” (ASAI¹⁴, Lefloch et al. 2018). This figure reveals that HCNH^+ is only abundant in the early phases of low-mass star formation. During the Class 0 phase, L1527 is the only

Class 0 object showing HCNH^+ emission. This trend is consistent with our finding that the HCNH^+ abundance decreases from the starless phase to the protostellar phase (see Fig. 12).

HCNH^+ is not detected in the Class I object, SVS13A, or the shocked regions, L1157-B1 and L1148-R2. We also note that HCNH^+ was not detected in the line survey toward the protoplanetary disk, AB Aur (Pacheco-Vázquez et al. 2015). This indicates that HCNH^+ is not prominent in late stages of low-mass star formation.

¹⁴ <https://www.iram.fr/ILPA/LP007/>

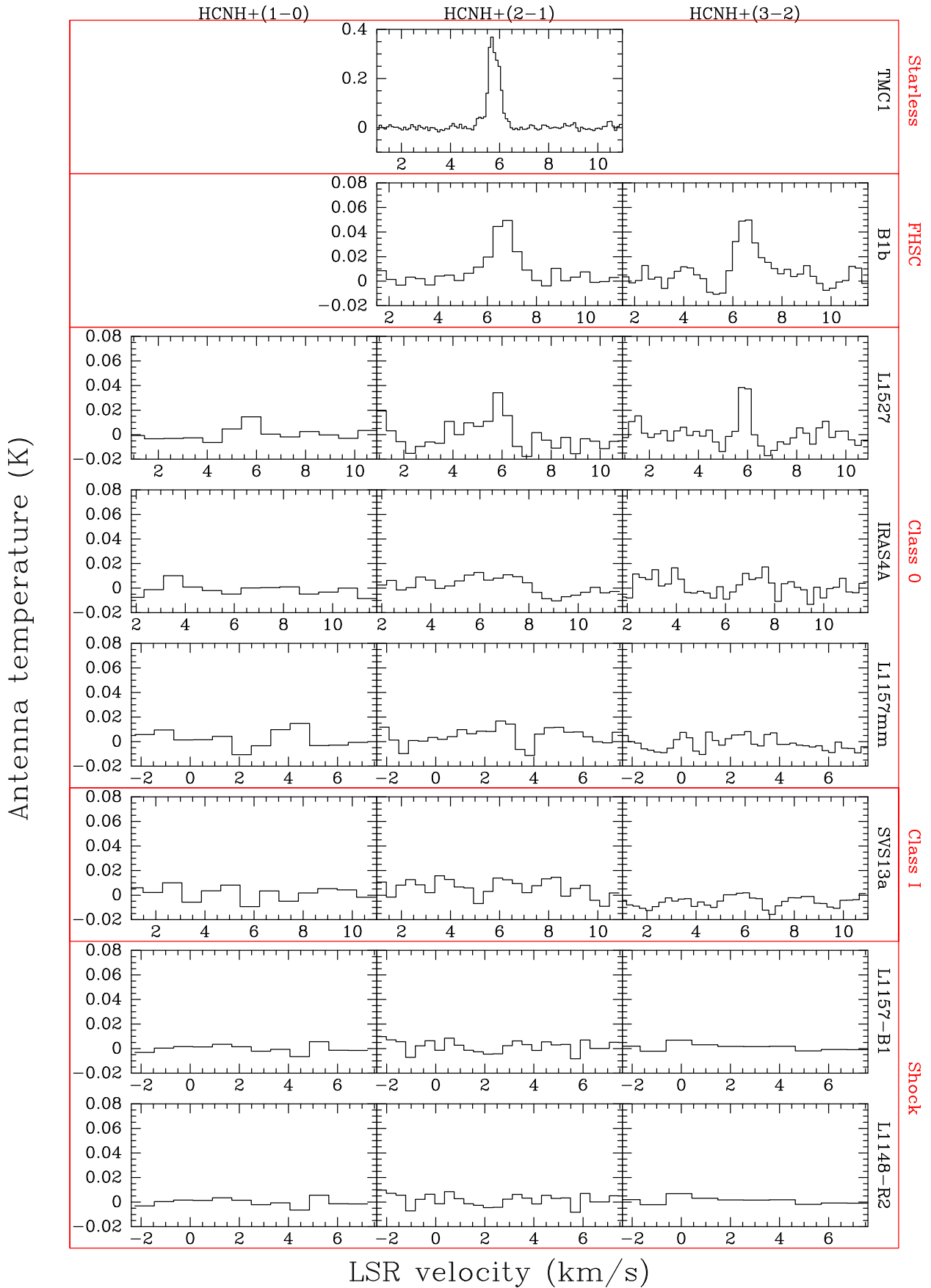


Fig. B.1. ASAI HCNH^+ spectra of TMC1, B1b, L1527, NGC1333-IRAS4A, L1157mm, NGC1333-SVS13a, L1157-B1, and L1148-R2, which represent different evolutionary stages, including starless cores, first hydrostatic cores, Class 0 protostars, Class I protostars, and shocked regions. HCNH^+ (1–0), (2–1), and (3–2) are shown in the first, second, and third columns. The source name is indicated on the right side.

Appendix C: Updated chemical models

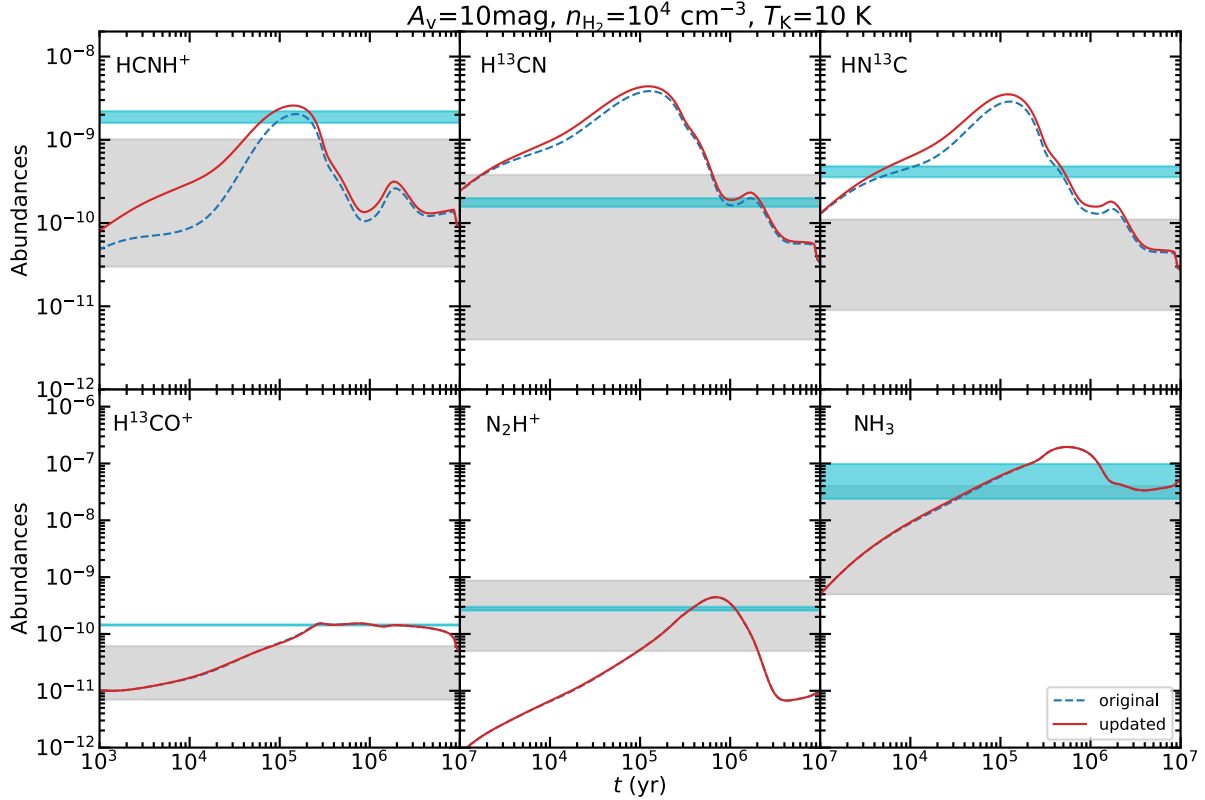


Fig. C.1. Molecular abundances relative to H_2 as a function of time, calculated from *Chempl* (Du 2021). The dashed blue lines represent the modeling results in Sect. 4.2, while the solid red curves represent the modeling results obtained when including reaction (7) in the underlying chemical network. The observed molecular abundances in our studies are indicated by the gray shaded regions, while the molecular abundances in TMC1 (Agúndez & Wakelam 2013) are indicated by the cyan shaded regions. The other physical conditions are indicated at the top of this figure.

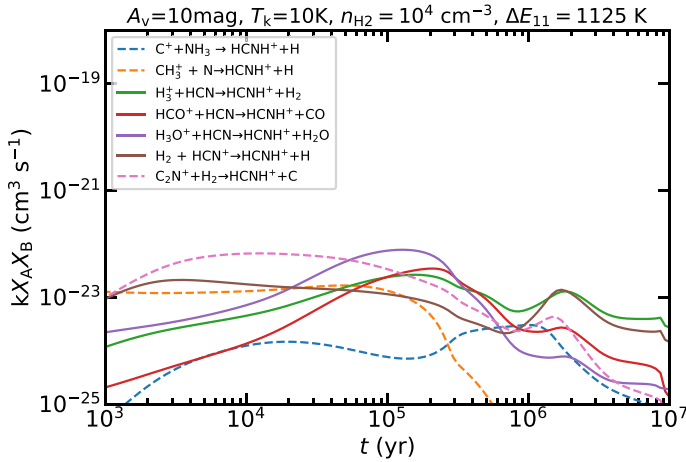


Fig. C.2. Same as Fig. 22 but when including reaction (7) in the underlying chemical network.

As demonstrated in Sect. 4.2, reaction (7) appears to play an important role in the formation of HCNH^+ . Consequently, we have embarked on an exploration of chemical models, augmenting the existing chemical network with the inclusion of reaction (7). The results of this endeavor are displayed in Fig. C.1, which showcases modeling results under fixed physical conditions with $A_V=10$ mag, $T_g=10$ K, and $n_{\text{H}_2} = 10^4 \text{ cm}^{-3}$. Compared to the results with the chemical network without reaction (7), we find that HCNH^+ , H^{13}CN , and HN^{13}C can reach higher

abundances in the updated chemical models. Especially for a simulated timescale of $\lesssim 10^5$ yr, HCNH^+ abundances are much higher in the updated chemical models. The most substantial discrepancy emerges around 10^4 yr, exhibiting a factor of ~ 5 difference.

We also revisit the formation rates with the updated chemical networks as in Fig. 22. The updated results are shown in Fig. C.2. Compared to Fig. 22, the formation rate of reaction (7) in the updated chemical model is significantly reduced by about four orders of magnitude. This is because reaction (7) causes the rapid decrease of the C_2N^+ abundance in early time and the C_2N^+ abundance is about four orders of magnitude lower than in Fig. 22. It is still worth noting that the formation rate of reaction (7) is still high before 10^5 yr when the freeze-out process becomes more important. These facts demonstrate that reaction (7) can make significant contributions to the formation of HCNH^+ at least at a simulated timescale of $< 10^5$ yr.

On the other hand, our findings regarding the overall abundance evolution remain remarkably consistent beyond 10^5 yr in Fig. C.1, because the freeze-out process becomes dominant in driving the abundance evolution. Because our targets are expected to have ages of $\gtrsim 10^5$ yr, the consistency between the models further strengthens the reliability of the results outlined in Sect. 4.2. The abundances of H^{13}CO^+ , N_2H^+ , and NH_3 are identical across the simulated timescales from both sets of modeling results, implying that reaction (7) plays a negligible role in determining the abundances of these particular species.